Enhanced Silicon-Graphene Photodetectors for Low-Noise, High-Sensitivity Applications

by

Federico G. De Geronimo

A dissertation submitted in partial fulfillment
of the requirements for the degree of
Doctor of Philosophy
(Climate and Space Sciences and Engineering)
in the University of Michigan
2026

Doctoral Committee:

Professor Nilton O. Renno, Chair
Associate Research Scientist Roger De Roo
Professor Fred Terry
Assistant Research Scientist Yun Zhang

Federico G. De Geronimo

fedegero@umich.edu

ORCID iD: 0000-0001-8158-8245

© Federico G. De Geronimo 2026

Dedication

To my wife, Warda
my parents, Marcella and Gianluigi
and my siblings, Francesca and Giovanni
Without whom none of my success would be possible

Acknowledgements

This work would not exist without the guidance of Dr. Nilton O. Rennó. As my research advisor, he shaped not only how I think about science, but how I approach challenges far beyond the lab. His mentorship has been one of the great privileges of my graduate years, and I am deeply grateful.

I owe a great deal to the staff of the LNF, and especially to Dr. Jorge Barreda. His patience, technical mastery, and willingness to engage with every stage of the fabrication process — from training to troubleshooting to design — gave me a genuine foundation in nanofabrication. I walked away from that work with a field I hadn't expected to love.

I am also grateful to BlueHalo and to Andy in particular for taking a chance on a first-time intern. That experience opened more doors than I could have anticipated, and the opportunities that followed were built directly on what I learned there.

To Campb, Conor, Elias, Eze, Matt, Samir, Saj, Steve, and Zach — thank you for staying close across the miles and the time zones. That kind of friendship doesn't go unnoticed, and it kept me grounded more than you know.

To my wife, Warda: thank you for standing beside me through every difficult stretch of this. And to my mother, Marcella, and the rest of my family — thank you for being my most constant source of encouragement.

Finally, to my father: there are no words adequate to describe what your example has meant to me, as an engineer and as a person. I owe you more than I can say. *Grazie, Papi.*

Table of Contents

Dedication ii

Acknowledgements iii

List of Figures vii

Abstract xii

Chapter 1 Introduction and Preliminary Investigations 1

1.1 Photodetectors Operating Principle 1

1.2 Photodetector Figures of Merit 3

1.3 Graphene as a Photodetector Material 7

1.3.1 Broadband Graphene-based Photodetector Fabrication & Testing 9

1.4 Graphene-Enhanced Photodetectors 13

1.4.1 Literature Review of Graphene-Enhanced Photodetectors 13

1.5 Scope of this Research 15

1.6 References 18

Chapter 2 Graphene-Silicon Device Architecture and Fabrication 21

2.1 Overview of Device Architecture 21

2.1.1 High-Gain Silicon-Graphene Detector Architecture 21

2.1.2 Silicon-Graphene Device Operating Principle 22

2.2 Overview of Device Fabrication Process 24

2.2.1 Device Design Preparation & Lithography Mask Etching 25

2.2.2 Silicon Wafer Etching & Dicing 26

2.2.3 Graphene Deposition 28

2.2.4 Graphene Patterning & Etching 31
2.2.5 Metal Electrode Patterning & Deposition 33
2.2.6 Device Packaging 35
2.3 Device Quality & Operation Verification 36
2.3.1 Visual Inspection of Devices 37
2.3.2 Raman Spectroscopy Analysis of Deposited Graphene 39
2.3.3 Minority Lifetime Measurements & Back Gate Current Measurements 40
2.3.4 High-Gain & Enhanced Responsivity Verification 42
2.4 References 46
Chapter 3 Low-Noise Stabilization Mechanism to Enhance the Performance of High-Gain Silicon-Graphene Photodetectors – F. De Geronimo, N. Renno 48
3.1 Abstract 48
3.2 Motivation & Proposed Stabilization Mechanism 49
3.2.1 Motivation 49
3.2.2 Proposed Stabilization Mechanism 49
3.3 Testing Setup & Device Characterization 51
3.3.1 Room Temperature Optical Characterization Test Setup 51
3.3.2 Variable Temperature Optical Characterization Test Setup 53
3.3.3 Characterization Tests 55
3.4 Results 56
3.4.1 Device Dark Current Measurements at Various Temperatures 56
3.4.2 Device Photoresponse with Constant Incident Laser Power at High and Low Temperatures 57
3.4.3 Room Temperature Laser Modulation with and without “Noisy” White Light 58
3.5 Conclusion & Future Work 59
3.6 References 60

Chapter 4 Silicon-Graphene Quadrant Detector for Precision Low-Flux Laser Alignment 62
4.1 Abstract 62
4.2 Introduction 63
4.3 Quadrant Detector Device Architecture 63
4.3.1 Quadrant Detector Device Design 63
4.3.2 Circuit Design & Test Setup 65
4.4 Device Characterization Setup 66
4.4.1 Testing Setup & Laser Profile Verification 67
4.5 Results 69
4.5.1 Device Dark Current & Noise 69
4.5.2 Device Active Area & Responsivity 71
4.5.3 Laser Position Sensitivity 73
4.6 Conclusion & Future Work 75
4.7 References 76
Chapter 5 Conclusion and Future Investigations 78
5.1 Summary of Key Contributions 78
5.2 Limitations of Current Achievements 80
5.3 Recommendations for Future Studies 81
5.4 Final Remarks 83

List of Figures

Figure 1. Spectral responsivity of silicon (Si), germanium (Ge), and indium gallium arsenide (InGaAs) photodetectors as a function of incident wavelength. Silicon exhibits strong response in the visible spectrum with a cutoff near ~1100 nm, germanium extends sensitivity into the near-infrared up to ~1600 nm, and InGaAs provides high responsivity across the near-infrared region (~900–1600 nm). The curves highlight the dependence of detector performance on material bandgap and illustrate the need for different semiconductor materials to achieve broadband optical detection. Reproduced from [2]. 4

Figure 2. Specific detectivity (D*) of representative photodetector materials as a function of incident wavelength. The curves illustrate the spectral dependence of detector sensitivity, with each material exhibiting peak performance within a wavelength range dictated by its bandgap. The BLIP (background-limited infrared photodetector) limit is the theoretical sensitivity threshold where the infrared detector's performance is constrained by the ambient background photon radiation rather than its own internal noise. Reproduced from [4]. 5

Figure 3. Schematic of graphene's band structure near the Dirac point, illustrating the linear energy-momentum dispersion (Dirac cones) of the valence and conduction bands. Upon illumination, an incident photon promotes an electron from the valence band to the conduction band via interband absorption, leaving behind a hole. This vertical transition in momentum space reflects graphene's zero bandgap and enables broadband optical absorption across a wide range of wavelengths. Reproduced from [8]..... 7

Figure 4. Schematic of the graphene photodetector architecture adapted from Mueller et al. (2010). Interdigitated source and drain electrodes are patterned directly on top of a graphene channel to minimize carrier transit distance and maximize collection efficiency. Reproduced from [12]. 10

Figure 5. Optical microscope image (**left**) and atomic force microscopy (AFM) image (**right**) of patterned electrode fingers in our in-house fabricated graphene-based photodetector. The optical image shows interdigitated metal source and drain electrodes defined across a graphene region that is not optically visible. The corresponding AFM image resolves the surface topography of the metal fingers, confirming the electrode geometry, uniformity, and nanoscale edge definition critical for minimizing contact resistance and maximizing device responsivity. 12

Figure 6. The device we developed uses p-doped silicon (colored in blue) as the light-absorbing semiconductor material and a high-gain graphene channel (colored in black) as the transparent signal amplifying layer..... 22

Figure 7. Illustration of the quantum gain, or Quantum Carrier Reinvestment mechanism. **(A)** Incident photons indicated by the red arrow generate electron hole pairs in the depletion region. **(B)** The imposed potential rapidly separates the carriers and injects electrons into the graphene channel. These carriers are coupled until the corresponding coupled holes in the silicon recombine. **(C)** The electron moves extremely rapidly in the graphene, where it takes time t = τt for them to travel from one electrode to the other, allowing the carrier to be replaced multiple times by another electron from the source contact in a short time. The original electron, e_1, moves a distance X_{e1} to the drain contact and is replaced by electron e_2 that travels a distance X_{e2} from the source contact, resulting in an effective movement of one electron from source to drain. This occurs many times while the electron's position is coupled to the hole in the silicon. **(D)** Once the hole in the silicon recombines at t = τr, the electron in the graphene is no longer coupled to the position and moves to the drain contact, ending the gain process. 23

Figure 8. Silicon/SiO_2 wafer following selective SiO_2 etching used to define photodetector geometries. The device array is deliberately spaced to facilitate wafer cleaving into smaller dies for subsequent processing and integration steps. 27

Figure 9. (**Left**) Process flow illustrating the transfer procedure for Trivial Transfer graphene obtained from ACS. Reproduced from ACS Material. (**Right**) Photograph of the graphene sheet immersed in deionized (DI) water at the solvent bench prior to transfer onto the target device substrate. 29

Figure 10. Images of graphene-PMMA wet transfer results onto the detector surface. (**Left**) Unsuccessful transfer showing significant air bubble formation and folding of the graphene-PMMA film across the active detector region, which can degrade device performance and film continuity. (**Right**) Successful transfer exhibiting good film uniformity across the graphene-PMMA sheet with minimal trapped air bubbles and improved coverage of the detector area. 30

Figure 11. Image of the device following acetone soaking and PMMA removal, leaving behind the transferred graphene layer on the detector surface. The graphene film demonstrates good uniformity and consistent coverage across the detector regions, indicating a successful transfer and cleaning process. 31

Figure 12. (**Left**) Single-element detector device we fabricated showing patterned graphene in the electrode regions prior to metal deposition. The graphene transferred over the light blue silicon (Si) window is not visible due to its optical transparency. (**Right**) Fabricated quad-cell detector featuring graphene strips transferred across the light-colored arrow-shaped Si windows for photodetection operation. 33

Figure 13. (**Left**) Microscope image of the fabricated quad-cell detector following metal electrode patterning and deposition. The electrodes are accurately aligned around the detector active regions and are designed with sufficient pad area to support subsequent wire bonding operations. (**Right**) Photograph of the fully fabricated detector prepared for the next fabrication stage, packaging and integration. 35

Figure 14. (**Left**) Completed device mounted in a leadless chip carrier (LCC) and secured using Kapton tape for stable electrical interfacing during testing. (**Right**) Optical microscope image showing wire bonds connecting the contact pads to the quadrant photodetector, enabling independent electrical access to each quadrant. 36

Figure 15. Microscope image of a prototype wire bonded single silicon-graphene detector. The patterned graphene area (purple) was designed to maximize the contact area between the graphene and the source/drain electrodes. The gate contact is not shown here. 36

Figure 16. (**Left**) Example of improperly developed graphene fingers following lithography, identified by rainbow-colored streaking, residual photoresist, and poorly defined feature edges. (**Right**) Correctly developed sample exhibiting sharp graphene finger features and uniform pattern definition. 38

Figure 17. Detector yield across four fabricated samples, each containing multiple individual detectors. A detector was classified as "good" if no visible defects were observed during post-fabrication inspection. All detectors categorized as "good" were subsequently electrically tested and confirmed to be operational. The results demonstrate a progressive improvement in fabrication yield across successive samples. 39

Figure 18. Raman spectra of transferred graphene measured on SiO_2 (top) and Si (bottom) substrates. Distinct graphene G and 2D peaks are observed near ~1580 cm^{-1} and ~2680 cm^{-1}, respectively, confirming the presence of graphene following transfer. Differences in peak intensity between the two spectra arise from substrate-dependent effects. 40

Figure 19. Recombination time as a function of incident optical power. The recombination time was extracted from the decay of the detector signal following optical modulation at each incident power level. The measured trend shows how carrier recombination dynamics vary with illumination intensity, providing insight into the minority carrier lifetime and its influence on detector gain and response time. 41

Figure 20. Back-gate current measurements for representative silicon-graphene detectors. The measured response follows diode-like behavior, indicating that carriers are injected across the silicon-graphene interface and supporting the proposed gain mechanism. Detectors E2, D6, and D9 are labeled according to their row and column positions on the fabricated detector sample. 42

Figure 21. Time-domain photoresponse of detector E2 under illumination from a modulated laser source. The measured transimpedance amplifier output voltage was converted to photocurrent using the 2 kΩ feedback resistor. The photocurrent was subsequently zeroed by subtracting the initial measured value, and the response is plotted as a function of time with the initial measurement point shifted to t=0 s. The incident laser was modulated between approximately 45 nW and 225 nW optical power, producing the periodic photocurrent variations observed in the signal. The detector clearly resolves the optical modulation, demonstrating its ability to detect low-flux, time-varying optical signals. 43

Figure 22. Responsivity as a function of incident optical power for multiple fabricated silicon-graphene photodetectors under 785 nm laser illumination, compared with the results of Liu and Kar (2014). Detectors are identified by their row-number and column-letter position on the

substrate. Measured devices exhibited higher responsivity and a steeper increase in responsivity at lower incident powers compared to the literature. 45

Figure 23. Extrapolated responsivity trends showing the average performance of all operational detectors, the highest-performing detector, and the results from Liu and Kar (2014). The extrapolation suggests responsivities up to 2–3 orders of magnitude greater than previously reported values at picowatt-level incident powers. 46

Figure 24. The detector design and associated stabilization mechanism electronics. The source is connected to the source capacitor (C_S) and the current source (I_S), which help regulate the source voltage (V_S). The drain is connected to the zeroing resistor (R_Z), the zeroing voltage (R_V), the feedback capacitor (C_F) and resistor (R_F), the user-set drain voltage (V_{DD}), the true drain voltage (V_D), and the output voltage of the system (V_{OUT}). 50

Figure 25. Schematic of the optical characterization setup used to evaluate the silicon-graphene photodetectors. A 635 nm laser diode, driven by a commercially available laser driver and modulated using the Analog Discovery 3 waveform generator, was focused onto the device-under-test (DUT) through a three-lens aspheric optical system. The DUT was mounted on a three-axis translation stage for precise alignment of the laser spot onto the detector active area. The stabilization circuit controlled the drain-source bias, while the output photoresponse was measured using the oscilloscope functionality of the Analog Discovery 3. 53

Figure 26. Optical testing setup used for device characterization in the temperature chamber. Blue desiccant beads placed in plastic bowls are used to control humidity within the enclosure, while a Bluetooth temperature sensor (white component to the left of the setup) monitors the local thermal environment during measurements. Foam padding beneath the optical breadboard helps dampen vibrations, particularly during temperature chamber cooldown, ensuring stable and low-noise data acquisition. A thick metal ribbon was also used to provide a robust common ground between the inside and outside of the chamber. 54

Figure 27. (**A**) Dark Current FWHM with and without the stabilization mechanism at various temperatures. The stabilization mechanism effectively reduces noise across the entire tested temperature range. (**B**) Dark Current with and without the stabilization mechanism at various temperatures. The variability in dark current without the stabilization mechanism is visibly greater than that with stabilization. 57

Figure 28. Response spectrum of the detector when (**A**) illuminated by only the low frequency white light, (**B**) illuminated by the high frequency modulated laser, and (**C**) illuminated by both the low frequency white light and the high frequency modulated laser. 58

Figure 29. Microscope image of our novel quadrant detector device. The dark background region is the SiO2, the yellow regions are the Ti/Au electrodes, the light blue arrow regions are the silicon windows, and the purple strips are the areas where the graphene was patterned into parallel strips. Each graphene strip is 3 μm wide, and the strip separation is 2 μm. The total effective length of each strip is approximately 100 μm. 64

Figure 30. Experimental optical characterization setup used for quadrant detector testing. (**Left**) Optical setup consisting of a lens tube assembly used to focus the laser to an

approximately 20 μm spot size, the device under test (DUT) mounted on a three-axis translation stage for precise positioning, and electrical connections routed from the DUT to custom circuits housed on breadboards compatible with the Analog Discovery 3. (**Right**) The same setup shown with the light-blocking enclosure used to ensure dark measurement conditions during dark current characterization with overhead lighting turned off. 67

Figure 31. Three-dimensional intensity profile of the focused laser spot measured using a CMOS camera. The spatial dimensions are shown in microns, with the minimum spot diameter measured to be approximately 20 μm at focus. The beam exhibits slight asymmetry, likely arising from minor optical aberrations and alignment imperfections within the imaging system.69

Figure 32. The dark current noise spectrum is plotted for the four quadrants. The noise from the electronics (i.e. replacing the device with a resistor of value equal to the graphene resistance) is also plotted to verify that the visible noise contributions are indeed from the quadrant detector. Peaks near 60 Hz are likely due to induced noise from the utility power during testing. 70

Figure 33. (**Left**) Detector response extracted from a raster scan of entire detector area using a 20 μm wide 635 nm 2 μW laser. The source (S) and drain (D) are labeled for each quadrant, and the lower right quadrant has an image of our detector overlayed to show that features like the gold electrodes and SiO_2 areas are captured in the scan. (**Right**) Comparison of device active areas for rotational and X-Y symmetry device configurations. For rotational symmetry, the drain and source alternate as you go around the device (D, S, D, S, etc.), while for X-Y symmetry, the sequence of drain and source is D, D, S, S, etc..... 72

Figure 34. (**Left**) Normalized X position signal as a function of horizontal displacement along the optical-center cut of the quadrant detector. (**Right**) Normalized Y position signal as a function of vertical displacement along the optical-center cut. Each plotted data point represents the average detector response over 30 modulation pulses. In both panels, the solid black curves represent the measured detector response, while the red dashed lines indicate least-squares linear fits. The slopes of the fits define the normalized position sensitivities, and deviations from linearity are used to quantify the detector nonlinearity. The mean normalized signal standard deviation was 0.0036 for the X-position response and 0.0023 for the Y-position response..... 74

Abstract

This dissertation investigates hybrid silicon-graphene photodetectors for low-noise, high-sensitivity optical sensing applications. Although silicon photodetectors are widely used because of their mature fabrication infrastructure, low cost, and strong optical absorption in the visible spectrum, their performance is fundamentally limited in low-flux applications by modest responsivity, dark current noise, and trade-offs between gain, sensitivity, and stability. These limitations motivate the development of detector architectures that preserve the advantages of silicon while introducing new mechanisms for signal enhancement.

Graphene offers exceptional carrier mobility, broadband optical properties, and compatibility with semiconductor processing, making it an attractive material for enhancing silicon-based photodetectors. However, graphene-only photodetectors suffer from low optical absorption, limited responsivity, and fabrication complexity. This work therefore investigates whether a hybrid silicon-graphene architecture can achieve high responsivity while maintaining low noise, environmental stability, and scalability to multi-pixel detector systems.

To address this question, silicon-graphene photodetectors were designed, fabricated, and characterized using an in-house process that included silicon processing, graphene transfer and patterning, metal electrode fabrication, device packaging, and optical/electrical testing. Initial studies of graphene-only detectors informed the transition to a hybrid architecture in which silicon serves as the primary light-absorbing material and graphene functions as a high-mobility transport and gain layer.

Experimental results demonstrated high-gain silicon-graphene photodetectors with measured responsivities approaching 500 A/W under low optical power illumination. A novel stabilization mechanism reduced dark current noise power by approximately 2–4x over temperatures from -5°C to 55°C while maintaining high optical gain. The stabilized architecture was further extended to a silicon-graphene quadrant detector using an L-shaped graphene geometry, achieving responsivities of approximately 10–23 A/W per quadrant with low cross-talk and linear position sensitivity.

This research establishes a framework for fabricating, stabilizing, and scaling silicon-graphene photodetectors for high-sensitivity optical sensing and precision alignment applications.

Chapter 1 Introduction and Preliminary Investigations

1.1 Photodetectors Operating Principle

Photodetectors are devices that convert light (e.g., photons) into an electrical signal through the photoelectric effect. These devices can be made in many different array sizes and from many materials, but the most common photodetector architecture uses semiconductor materials. This is due to semiconductor's intrinsic bandgap, where an incident photon with sufficient energy can generate electron-hole pairs. These photo-generated carriers are subsequently separated and collected under the effect of an applied electric field, while this photoresponse is measured by dedicated low-noise electronics. The photoresponse of the device is proportional to the number of carriers generated in the detector material, which in turn is heavily dependent on the flux of incident light on the detector.

The absorption of light in a semiconductor is governed by the material's band structure and optical properties. Photons with energy $h\upsilon \geq E_g$, where h is Planck's constant, υ is the frequency of the incident light, and E_g is the energy bandgap of the semiconductor material, can move electrons from the valence band to the conduction band, leaving a hole in the valence band. The efficiency of this process is dependent on the absorption of the material and the penetration depth of the incident light, both functions of the light frequency or wavelength. As a result, the semiconductor material for a specific application is selected based on the frequency band or wavelengths of interest.

Most semiconductor photodetectors are either photoconductive or photovoltaic. In photoconductive devices, an external bias is applied across the semiconductor material, and illumination increases the number of carriers in the material. As the carriers in the material increase, the conductivity of the material increases as well. Consequently, the current of the device can be measured and the photoresponse can be extracted as a function of incident light and the applied external bias. One key feature of photoconductive devices is that they may enable internal gain, which arises when the carrier lifetime exceeds the carrier transit time across the device. In this regime, a single carrier can contribute multiple times to the generated photocurrent until it recombines, enabling a gain $G > 1$.

Photovoltaic devices typically rely on a depletion region where carriers are efficiently generated and separated. Schottky junctions, p-n junctions, and heterointerfaces are key enablers of these photovoltaic devices. They can operate either in photovoltaic mode, where no voltage is applied across the junction and the device relies on the depletion region built-in voltage, or in photoconductive mode (reverse-bias mode), where a voltage is applied across the junction to increase the depth of the depletion region. Devices operating in photovoltaic mode typically exhibit lower internal gain because carrier collection occurs primarily within the built-in depletion region without substantial photoconductive amplification. However, they are generally characterized by much lower noise than photoconductive devices due to lower dark current. Indeed, devices operating in photoconductive mode are more efficient due to the larger size of the depletion region but are characterized by higher noise due to the higher dark current.

These differences lead to distinct performance trade-offs. Photoconductive detectors are often favored in applications requiring high gain, particularly when signal levels are low, but at the cost of increased noise (i.e. lower signal-to-noise ratio (SNR)) and potentially slower response

times. Photovoltaic detectors are well-suited for higher SNR and higher speed applications where stability and bandwidth are critical.

Understanding the differences between photoconductive and photovoltaic detectors is critical for evaluating which architecture is preferable for a specific application. These operational modes provide a useful framework for analyzing existing and emerging detector technologies, where it is not uncommon to incorporate aspects of both photoconductive and photovoltaic detectors in the design. Hybrid graphene-based photodetectors, the subject of this thesis, offer unconventional transport mechanisms and gain processes that blur the line between these two operating modes.

1.2 Photodetector Figures of Merit

The performance of photodetectors is assessed using standard figures of merit (FOMs) that measure their sensitivity, efficiency, speed, and noise characteristics. These metrics can be used to compare device designs and materials. They are crucial for understanding the trade-offs that influence photodetector design and operation.

One key performance metric is **responsivity (R)**, defined as the ratio between the photoresponse of the detector (I_{ph}) and the incident optical power on the detecting area (P_{opt}) [1],

$$R = \frac{I_{ph}}{P_{opt}}. \tag{1.1}$$

Responsivity quantifies how efficiently incident light is converted into an electrical signal and is typically quantified at specific wavelengths of light. A responsivity spectrum can be generated for different detecting materials by sweeping the wavelength of incident light – the responsivity spectra for Silicon (Si), Germanium (Ge), and Indium Gallium Arsenide (InGaAs) are illustrated in Figure 1.

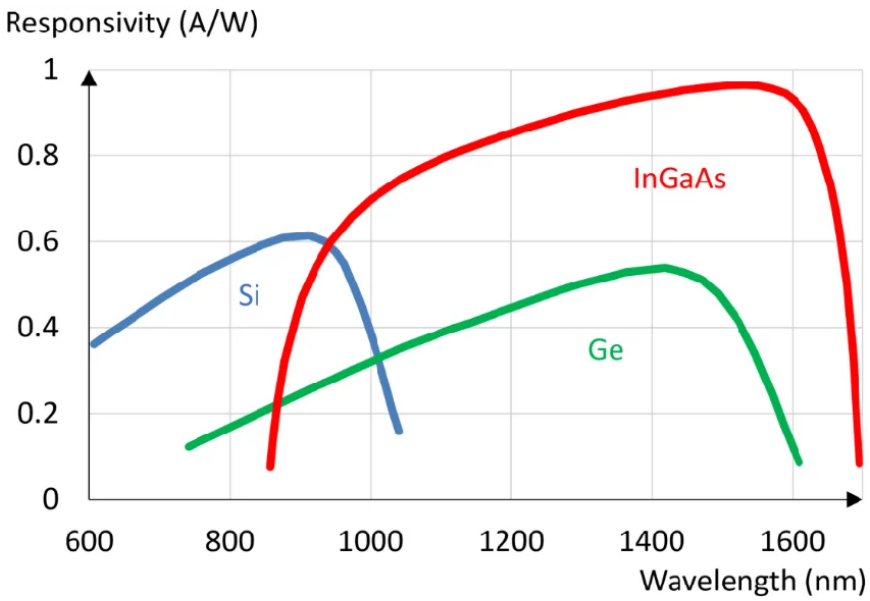


Figure 1. Spectral responsivity of silicon (Si), germanium (Ge), and indium gallium arsenide (InGaAs) photodetectors as a function of incident wavelength. Silicon exhibits strong response in the visible spectrum with a cutoff near ~1100 nm, germanium extends sensitivity into the near-infrared up to ~1600 nm, and InGaAs provides high responsivity across the near-infrared region (~900–1600 nm). The curves highlight the dependence of detector performance on material bandgap and illustrate the need for different semiconductor materials to achieve broadband optical detection. Reproduced from [2].

Responsivity is closely linked to **external quantum efficiency (EQE)**, which is the ratio of collected charge carriers to incident photons. The relationship between responsivity and EQE is

$$R = \frac{q\lambda}{hc} \cdot EQE \ , \tag{1.2}$$

where q is the elementary charge, λ is the incident wavelength, h is Planck's constant, and c is the speed of light [3].

In darkness, photodetectors have a non-zero current known as the **dark current (I_d)**. This current comes from thermally generated carriers, leakage pathways, and material defects. Dark current is significant because it directly adds to noise and limits the smallest signal that can be detected. The main noise source linked to dark current is shot noise, which arises from the random and discrete nature of generated charge carriers, expressed as

$$i_n = \sqrt{2qI_d\Delta f} \ , \tag{1.3}$$

where Δf is the measurement bandwidth [1].

The sensitivity of a photodetector is often measured using **noise-equivalent power (NEP)**. NEP is the incident optical power needed to produce a signal equal to the root-mean-square noise level within a 1 Hz bandwidth [3]

$$NEP = \frac{i_n}{R}, \tag{1.4}$$

where R is the responsivity and i_n is the dark current noise. A lower NEP indicates a more sensitive detector. **Specific detectivity (D*)** is closely related to NEP, and normalizes detector performance by considering their active area (A) and bandwidth [1, 3]

$$D^* = \frac{\sqrt{A\Delta f}}{NEP}. \tag{1.5}$$

Specific detectivity is widely used to compare detectors of different sizes. Typical spectral D* values for common detector materials are shown in Figure 2.

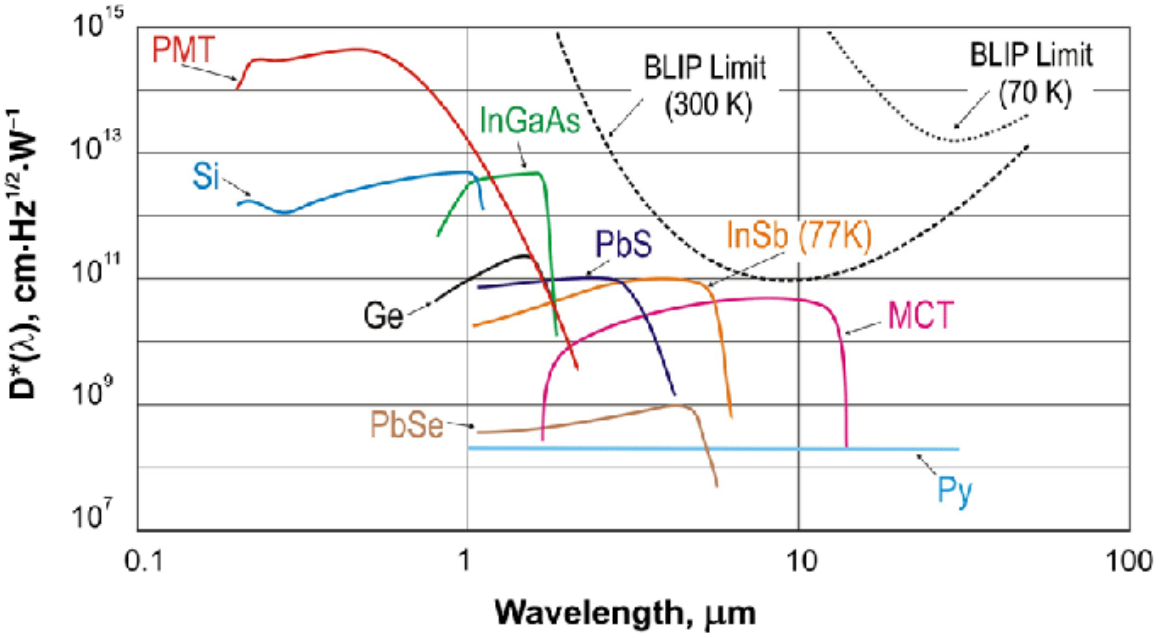


Figure 2. Specific detectivity (D*) of representative photodetector materials as a function of incident wavelength. The curves illustrate the spectral dependence of detector sensitivity, with each material exhibiting peak performance within a wavelength range dictated by its bandgap. The BLIP (background-limited infrared photodetector) limit is the theoretical sensitivity threshold where the infrared detector's performance is constrained by the ambient background photon radiation rather than its own internal noise. Reproduced from [4].

Another important parameter is the **signal-to-noise ratio (SNR)**, defined as the ratio of the photocurrent to the total noise current (i_n) [1]

$$SNR = \frac{I_{ph}}{i_n}, \tag{1.6}$$

which measures how well a photodetector can differentiate an incident signal from background noise. It is a critical FOM for low-flux applications.

Gain refers to the internal amplification of photocurrent within the detector, defined as the ratio of collected carriers to the number of absorbed photons. Gain mechanisms arise in photoconductors and avalanche photodiodes through carrier multiplication or extended carrier lifetime. In the case of extended carrier lifetime, the optical gain can be approximated by taking the ratio of the excess minority carrier lifetime (τ) and the carrier transit time (τ_T) [5]

$$G \approx \frac{\tau}{\tau_T}. \tag{1.7}$$

Finally, the **response time** of a photodetector is typically defined by the time constant associated with the -3 dB cutoff frequency f_{3dB} (or bandwidth), which is the frequency at which the detector's linear response drops to ~70% (or 50% in power) of its maximum value [6]. The bandwidth depends on factors such as carrier transit time, recombination lifetime, and RC time constants associated with the electronics. It sets the maximum speed at which the detector can respond to changing optical signals.

These figures of merit establish the fundamental performance limits of photodetectors. They reveal the essential trade-offs between responsivity, noise, gain, and speed. Understanding and optimizing these factors is crucial for developing new photodetector designs, especially in advanced material systems like graphene-based or graphene-enhanced devices.

1.3 Graphene as a Photodetector Material

Graphene has emerged as a promising material for state-of-the-art detectors because of its unique electrical and optical properties. It is a 2D material composed of a single layer of carbon atoms arranged in a hexagonal lattice. Unlike typical semiconductor materials, where the bandgap dictates the operation wavelengths or frequency band of the device, graphene exhibits zero bandgap and a linear energy-momentum dispersion near the Dirac point, as shown in Figure 3. This unique characteristic enables broadband absorption spanning from the ultraviolet to the terahertz regime, making graphene particularly attractive for applications requiring wide spectral coverage [7].

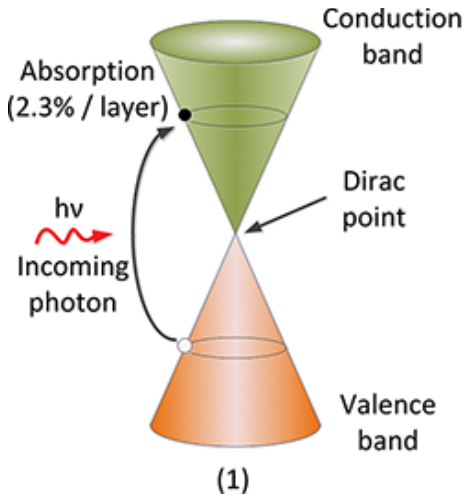


Figure 3. Schematic of graphene's band structure near the Dirac point, illustrating the linear energy-momentum dispersion (Dirac cones) of the valence and conduction bands. Upon illumination, an incident photon promotes an electron from the valence band to the conduction band via interband absorption, leaving behind a hole. This vertical transition in momentum space reflects graphene's zero bandgap and enables broadband optical absorption across a wide range of wavelengths. Reproduced from [8].

Moreover, graphene possesses extremely high carrier mobility, enabling photodetectors with exceptionally high bandwidth and rapid response time. Indeed, electron and hole mobilities $\mu > 10^6$ cm^2/V-s have been reported in the literature [7], while the mobility of electrons and holes in silicon reaches only 1,400 cm^2/V-s and 450 cm^2/V-s, respectively [9]. This exceptionally high

carrier mobility also has the potential to introduce a powerful internal gain mechanism when paired with a light-absorbing semiconductor substrate, as we will showcase in our research.

However, as a standalone light-absorbing material, graphene suffers from significant drawbacks that have prevented it from being widely adopted as a detector material. Most notably, graphene's absorption is limited to ~2.3% across the visible spectrum, primarily due to its atomically thin, two-dimensional structure [7, 10]. The low absorption of graphene limits the photoresponse of the material resulting in intrinsically low responsivity in devices that rely solely on direct photon absorption within the graphene layer [11].

In addition to limited absorption, graphene exhibits extremely short carrier lifetimes due to rapid carrier-carrier and carrier-phonon scattering processes. While these ultrafast dynamics enable high-speed operation, they also reduce the probability of carrier collection before recombination, further suppressing photocurrent generation. As a result, efficient carrier extraction requires carefully engineered device geometries with short transport distances, which can constrain device scaling and complicate integration into large-area or multi-pixel detector arrays. Furthermore, the absence of a bandgap limits the formation of strong built-in electric fields, often necessitating external biasing or complex junction engineering, which can introduce additional noise and reduce overall device stability.

To better understand these limitations in practice, our initial investigation was conducted by fabricating and characterizing graphene-based photodetectors using precisely patterned gold electrodes for optimal signal extraction. We present our findings of this preliminary investigation in the following section, as well as the motivation to pursue an alternate detector architecture composed of a graphene-semiconductor hybrid device.

1.3.1 Broadband Graphene-based Photodetector Fabrication & Testing

Despite the shortcomings of graphene as a standalone detector material such as limited absorption, the possibility of broadband absorption provided a compelling benefit for space-based sensing applications. Typically, space missions require broadband sensing capabilities to image targets at different wavelengths. To meet these requirements, multiple detectors, each optimized for a different narrow wavelength range, need to be housed on a spacecraft, requiring significant amount of space and mass. Graphene-based photodetectors may be able to eliminate the need for multiple detectors simply by housing one detector along with a grating or various optical filters for the wavelength of interest, significantly reducing the size, mass, and complexity of future spacecrafts.

Thus, we decided to initially pursue a promising graphene-based detector architecture based on the results of Mueller et al. (2010) [12], whose design is illustrated in Figure 4. The goal of our initial study was to determine the feasibility of this design with current nanofabrication techniques and characterize the detector across different wavelengths. Following this study, we would scale the architecture to a multi-detector array, moving towards a final device capable of being housed on future space missions.

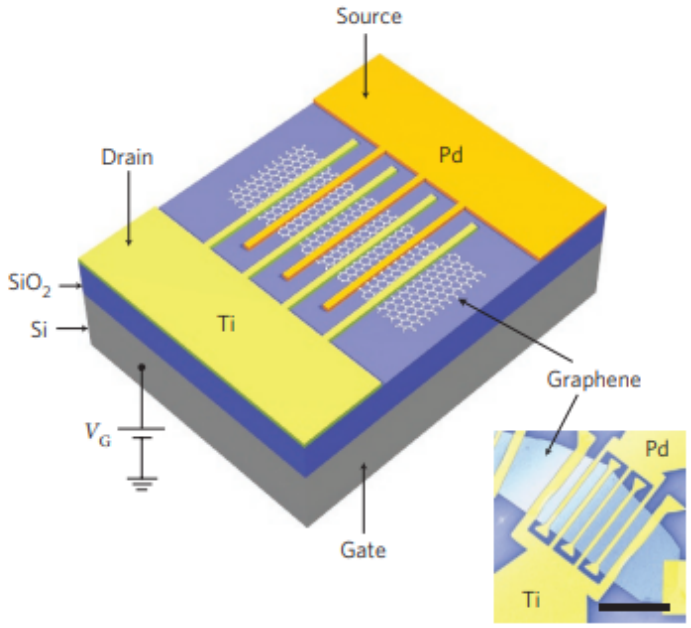


Figure 4. Schematic of the graphene photodetector architecture adapted from Mueller et al. (2010). Interdigitated source and drain electrodes are patterned directly on top of a graphene channel to minimize carrier transit distance and maximize collection efficiency. Reproduced from [12].

In the Mueller et al. (2010) design, graphene acts primarily as the light-absorber, with signal extraction occurring through the source and drain electrode fingers [12]. As light hits the graphene, carriers are generated and separated due to an applied bias across the source and drain electrodes.

The short carrier lifetime of graphene requires the electrode geometry to be as close as possible to the light-absorbing region. This minimizes recombination losses and enhances the response of the device. This requirement drives the need for the overlaid electrode fingers on the graphene region. Moreover, graphene's low absorption innately limits the response of this detector, and thus the electrode fingers are made as thin as possible (~250 nm wide) to maximize the area of the graphene exposed to the incident light.

Our detectors were fabricated in the Lurie Nanofabrication Facility at the University of Michigan. A p-doped silicon substrate with 100 nm of thermal oxide was used as the base for our

detectors. We initially deposited graphene using the tape method, in which adhesive tape is used to repeatedly peel layers of carbon from graphite to produce single-layer samples of graphene. However, this method quickly proved to be unreliable and time consuming due to our inability to control the shape and number of layers of the graphene, and thus we pivoted to purchasing commercially available graphene on Poly(methyl methacrylate) (PMMA). A wet transfer process using deionized (DI) water was used to deposit the graphene on diced SiO_2/Si substrates, and standard projection lithography processes were used to pattern the graphene into a simple rectangular shape.

Logistical limitations and quality issues quickly arose when patterning and depositing the small electrode fingers. First, E-beam lithography needed to be used to accurately pattern the small fingers. This process was very expensive and took a significant amount of time and resources, especially since the electrode material used for the source is different from the electrode material used for the drain (palladium (Pd) for the source compared to titanium (Ti) for the drain). This required two separate patterning sessions and metal depositions.

Moreover, the large electrode pads to which wire bonds would be connected needed to be patterned in gold to ensure proper bonding of the wire bonds. This required an additional step in the lithography machine and caused a 20 nm step between the SiO_2 region of the fingers and the gold electrode region of the fingers. During testing, we found this step to be the root cause of poor detector performance, as it caused broken contacts between the fingers and the gold pad. A microscope image and an Atomic Force Microscopy (AFM) image of these small gold fingers are shown below in Figure 5.

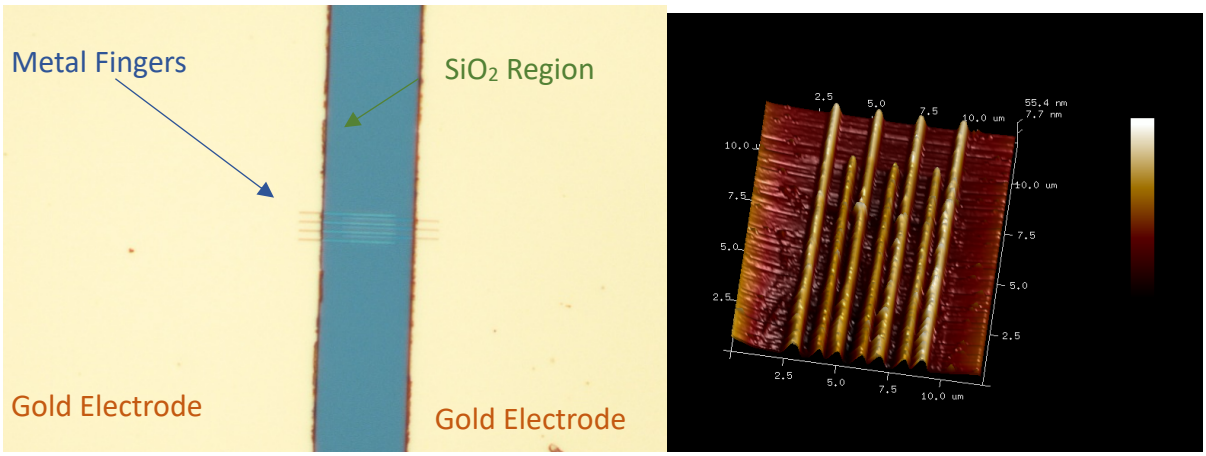


Figure 5. Optical microscope image (**left**) and atomic force microscopy (AFM) image (**right**) of patterned electrode fingers in our in-house fabricated graphene-based photodetector. The optical image shows interdigitated metal source and drain electrodes defined across a graphene region that is not optically visible. The corresponding AFM image resolves the surface topography of the metal fingers, confirming the electrode geometry, uniformity, and nanoscale edge definition critical for minimizing contact resistance and maximizing device responsivity.

The fabrication and performance challenges we faced highlighted a key limitation of relying on graphene as the sole photoactive material. While the architecture successfully demonstrated broadband operation and high-speed potential, the trade-offs in responsivity, manufacturability, and device reliability made it unsuitable for scalable deployment in its current form. In particular, the reliance on high-resolution lithography techniques and multiple metal deposition steps posed significant barriers to large-scale array fabrication, which is essential for imaging applications.

Consequently, this initial investigation motivated a **transition toward hybrid photodetector architectures**, in which graphene is integrated with conventional semiconductor materials to leverage the strengths of both systems. In these graphene-enhanced designs, the semiconductor serves as the primary light absorber, providing high quantum efficiency, while graphene functions as a high-mobility transport layer or gain medium. This approach preserves the broadband advantages of graphene while overcoming its intrinsic absorption limitations.

The following section introduces these graphene-enhanced photodetectors in detail, along with a comprehensive review of prior work in the field. Emphasis is placed on architectures that demonstrate improved responsivity, reduced noise, and compatibility with scalable fabrication techniques, ultimately guiding the design choices for the devices developed in this work.

1.4 Graphene-Enhanced Photodetectors

To overcome the limitations of graphene as a standalone detector material, research has focused on integrating high-quality graphene into existing semiconductor detector architectures. In such a configuration, the graphene no longer acts as the light-absorbing medium, rather it operates primarily as a transparent, high-mobility electrode, capable of inducing large internal gain into the system. Meanwhile, the semiconductor material serves as the primary photon-absorbing material.

This architecture leverages the strengths of both materials. The semiconductor material provides strong light absorption and efficient electron-hole pair generation due to its bandgap, while graphene facilitates rapid carrier transport and, if necessary for the application, internal gain. The result of these hybrid architectures is a high responsivity device capable of operating efficiently and at low incident powers, providing a promising detector platform for space applications and precision alignment needs. In the following section, we showcase much of the literature associated with silicon-graphene detectors that has shaped our research.

1.4.1 Literature Review of Graphene-Enhanced Photodetectors

Building upon the hybrid architecture described above, many investigations have focused on the integration of graphene into silicon photodetectors. This is due to the well-established lithography processes surrounding silicon devices, and the ability of graphene to be easily integrated into these architectures.

Graphene-silicon Schottky photodetectors are one of the most widely studied hybrid architectures in the literature. In these devices, graphene replaces the conventional metal contact and forms a rectifying junction with the silicon [13, 14]. In this configuration, incident light passes through the quasi-transparent graphene layer and generates electron-hole pairs in the silicon underneath. The built-in electric field at the junction subsequently separates the carriers. Compared to traditional metal-semiconductor photodiodes, these devices benefit from reduced optical losses at the contact due to a greater light collection area, as well as the ability to tune the barrier height via gating of the device or doping of the deposited graphene, enabling optimization of responsivity and dark current [13, 14].

An alternate architecture that has also been widely investigated is **photogating-enabled graphene-silicon photodetectors**, in which graphene's sensitivity to local electrostatic environments enhances signal response [15, 16]. In these devices, electron-hole pairs are created in the silicon, and one of the carriers is trapped in the bulk semiconductor material. The other carrier is rapidly collected in the graphene and alters the conductivity of the graphene until the trapped carrier in the silicon recombines. Since carriers in graphene can move at extremely high speeds (due to graphene's large carrier mobility), the injected carrier can be replaced multiple times before recombination of the trapped carrier occurs in the silicon. This leads to high internal gains exceeding 10^7 [16]. However, due to the mechanism's operating principle, it comes at the cost of higher dark current and reduced temporal response, as it relies on long carrier lifetimes and trap states. Much of the research presented in this thesis focused on the noise reduction and scalability of these high-responsivity devices.

In addition to electrical mechanisms, **optical enhancement strategies** have been studied to improve device performance. Since graphene's absorption is quite low, physical device

enhancements like plasmonic nanostructures, optical cavities, and waveguide-integrated geometries have been employed to increase light-matter interaction in the active region [11, 17]. These features allow for increased light absorption, leading to increased responsivity with minimal increase in temporal response.

Despite these promising approaches, noise and device stability remain significant challenges. Material defects, interface traps, and contamination during the fabrication process and transfer process all contribute to the noise of the device [18]. Moreover, in systems with high internal gain, this noise is amplified along with the signal, limiting overall signal-to-noise ratio. As a result, recent research has emphasized the need for device architectures and systems to reduce overall noise of these hybrid detectors without compromising their responsivity.

Overall, the literature demonstrates that hybrid silicon-graphene photodetectors offer a compelling path forward for high-sensitivity, low-power optical systems. However, research needs to be conducted to address the imbalance between the noise and gain of these systems. These limitations motivated our development of a noise-reducing stabilization mechanism.

1.5 Scope of this Research

Conventional silicon-based photodetectors are critical for a wide range of low-cost optical sensing applications, including imaging, precision metrology, and alignment systems due to their technological maturity, compatibility with standard semiconductor manufacturing processes, and resulting scalability. However, the performance of these systems is fundamentally limited by intrinsic material properties. Mainly, silicon photodiodes exhibit low responsivity, typically below 0.7 A/W in the visible spectrum, limiting sensitivity in low-flux environments [2]. Moreover, high responsivity silicon-based systems often suffer from high dark current noise, limiting overall sensitivity. These limitations restrict their effectiveness in applications requiring high sensitivity,

broad spectral response, or operation under low illumination conditions. As emerging technologies demand increasingly precise and low-noise optical detection, there is a need for photodetector architectures that can surpass the performance limits of conventional silicon-based devices.

Graphene offers a promising pathway as a detector-enhancing layer for silicon-based photodetectors due to its unique electronic and optical properties. As a two-dimensional material with zero bandgap and extremely high carrier mobility, graphene exhibits rapid carrier transport and response, while offering broadband absorption and detection, ranging from ultraviolet to long-wave infrared. Moreover, its compatibility with many different substrates and ease of integration into current semiconductor detector architectures makes it an attractive material as a transparent electrode for semiconductor-based detectors. These favorable properties have motivated extensive research into both graphene-based and graphene-enhanced photodetectors as candidates to overcome some of the limitations of current photodetector solutions.

Despite these impressive advantages, graphene-based photodetectors suffer from several fundamental challenges that have limited their widespread adoption. First, although graphene has broadband optical absorption properties, absorption across the spectrum is limited due its 2D nature. A single layer of graphene can only absorb approximately 2.3% of incident light, severely limiting its responsivity and sensitivity, especially in low-flux environments. Moreover, due to graphene's short carrier lifetime, short carrier collection lengths are required to minimize recombination losses. Electrode geometries optimized for rapid signal extraction tend to cover up much of the active area, impacting detector size and multi-detector array geometries. Finally, mechanisms that rely on graphene for internal gain not only amplify the photocurrent, but also the noise generated, providing little gain to existing semiconductor-based detector architectures. As a result, although graphene offers compelling advantages in speed and spectral coverage, existing

graphene-based and hybrid photodetector designs have yet to simultaneously achieve high responsivity, low noise, and scalable integration. This gap highlights the need for new device architectures and system-level approaches that can fully leverage graphene's properties while mitigating its inherent limitations.

In this thesis, we present (i) the design and characterization of prototypes of silicon-graphene photodetectors, (ii) a novel stabilization mechanism for silicon-graphene photodetectors to reduce noise and enhance performance, and (iii) a novel silicon-graphene quadrant detector architecture for high-accuracy laser position alignment. Our novel stabilization mechanism effectively reduces the dark current noise of silicon-graphene detectors while still enabling high-gain photoresponse. Improved performance is observed across a large range of temperatures and environmental conditions, showcasing the robustness and effectiveness of our stabilization mechanism. This stabilization mechanism is then incorporated into a novel quadrant detector architecture, to produce the first-of-its-kind multidetector silicon-graphene array. We verify the effectiveness of our quadrant detector as a position sensor with a focused laser system. Indeed, the quadrant detector prototype exhibits impressive positional accuracy and sensitivity, rivaling current silicon-based technologies.

This thesis is organized to systematically develop and evaluate silicon-graphene photodetector architectures, progressing from fundamental principles to device implementation and performance optimization. Chapter 1 introduces the operating principles of photodetectors, the motivation for improved performance beyond conventional silicon technologies, and the potential of graphene and graphene-enhanced systems, along with a review of relevant prior work. Chapter 2 describes the design and fabrication of the silicon-graphene device architecture, including processing steps such as graphene deposition, patterning, metallization, and device packaging, as

well as experimental verification of device quality and high-gain operation. Chapter 3 presents a low-noise stabilization mechanism developed to improve the performance of high-gain silicon-graphene photodetectors, along with detailed optical and thermal characterization results. Chapter 4 extends this work to a silicon-graphene quadrant detector architecture designed for precision low-flux laser alignment, including device design, read-out electronics, and comprehensive performance evaluation. Finally, Chapter 5 summarizes the key findings of this research and discusses future directions for optimizing silicon-graphene photodetector systems and expanding quadrant detector architectures for broader applications.

1.6 References

[1] S. M. Sze and K. K. Ng, Physics of Semiconductor Devices, 3rd ed. Hoboken, NJ, USA: Wiley, 2007.

[2] A. Carrasco-Casado and R. Mata-Calvo, "Free-space optical links for space communication networks," in *Springer Handbook of Optical Networks*, Springer, 2020, pp. 1057–1103.

[3] H. Marouf, N. Abdel Salam, E.-S. M. El-Rabaie, A. N. Z. Rashed, and K. M. ElKhamisy, "A Comprehensive Review of Photodetectors: Materials, Enhancement Techniques, Perspectives, and Recent Directions," Journal of Optics (India), 2025, doi: 10.1007/s12596-025-02779-4.

[4] J. Wojtas *et al.*, "Cavity-enhanced absorption spectroscopy and photoacoustic spectroscopy for human breath analysis," *International Journal of Thermophysics*, vol. 35, no. 12, pp. 2215–2225, Apr. 2014. doi:10.1007/s10765-014-1586-4

[5] H. Fang and W. Hu, "Photogating in low dimensional photodetectors," *Advanced Science*, vol. 4, no. 12, Oct. 2017. doi:10.1002/advs.201700323

[6] Y.-H. Deng, D. Van Thourhout, and Z. Hens, "Understanding and equivalence of response time measurements in photodetectors," *ACS Photonics*, vol. 13, no. 7, pp. 1752–1756, Apr. 2026. doi:10.1021/acsphotonics.6c00438

[7] F. Bonaccorso, Z. Sun, T. Hasan, and A. C. Ferrari, “Graphene photonics and Optoelectronics,” *Nature Photonics*, vol. 4, no. 9, pp. 611–622, Aug. 2010. doi:10.1038/nphoton.2010.186

[8] G. Sobon, "Application of 2D Materials to Ultrashort Laser Pulse Generation," in *Two-Dimensional Materials — Synthesis, Characterization and Potential Applications*, InTech, 2016. doi: 10.5772/63336.

[9] N. D. Arora, J. R. Hauser, and D. J. Roulston, “Electron and hole mobilities in silicon as a function of concentration and temperature,” *IEEE Transactions on Electron Devices*, vol. 29, no. 2, pp. 292–295, Feb. 1982. doi:10.1109/t-ed.1982.20698

[10] S. Schuler *et al.*, “High-responsivity graphene photodetectors integrated on silicon microring resonators,” *Nature Communications*, vol. 12, no. 1, Jun. 2021. doi:10.1038/s41467-021-23436-x

[11] F. H. Koppens *et al.*, “Photodetectors based on graphene, other two-dimensional materials and hybrid systems,” *Nature Nanotechnology*, vol. 9, no. 10, pp. 780–793, Oct. 2014. doi:10.1038/nnano.2014.215

[12] T. Mueller, F. Xia, and P. Avouris, “Graphene photodetectors for high-speed optical communications,” *Nature Photonics*, vol. 4, no. 5, pp. 297–301, Mar. 2010. doi:10.1038/nphoton.2010.40

[13] X. An, F. Liu, Y. J. Jung, and S. Kar, “Tunable graphene-silicon heterojunctions for ultrasensitive photodetection,” *Nano Letters*, vol. 13, no. 3, pp. 909–916, 2013.

[14] M. Casalino *et al.*, “Vertically Illuminated, resonant cavity enhanced, graphene-Silicon Schottky photodetectors,” *ACS Nano*, vol. 11, no. 11, pp. 10955–10963, Nov. 2017. doi:10.1021/acsnano.7b04792

[15] G. Konstantatos, M. Badioli, L. Gaudreau, J. Osmond, M. Bernechea, F. P. García de Arquer, F. Gatti, and F. H. L. Koppens, “Hybrid graphene-quantum dot phototransistors with ultrahigh gain,” *Nature Nanotechnology*, vol. 7, pp. 363–368, 2012.

[16] Liu F, Kar S. Quantum Carrier Reinvestment-induced ultrahigh and broadband photocurrent responses in graphene-silicon junctions. ACS Nano. 2014 Oct 28;8(10):10270-9. doi: 10.1021/nn503484s. Epub 2014 Oct 17. PMID: 25325405.

[17] E. Engel, A. Steiner, and P. Avouris, "Microcavity-Integrated Graphene Photodetector," *Nano Letters*, vol. 12, no. 7, pp. 3388–3393, 2012. doi: 10.1021/nl204512x

[18] M. D. Bhatt, H. Kim, and G. Kim, “Various defects in graphene: A Review,” *RSC Advances*, vol. 12, no. 33, pp. 21520–21547, 2022. doi:10.1039/d2ra01436j

Chapter 2 Graphene-Silicon Device Architecture and Fabrication

We begin this chapter by introducing the single-pixel silicon-graphene photodetector device architecture proposed by Liu and Kar (2014). We describe the internal gain mechanism that makes these detectors based on this architecture attractive for low-flux, high-sensitivity applications. This internal gain mechanism is present in the quadrant detectors we fabricated (more details are provided in Chapter 4). In Chapter 2.2, we outline the detailed fabrication process we developed to make these detectors in-house, starting with mask fabrication and ending with device packaging. Finally, in Chapter 2.3, we detail the various quality control steps we took to ensure high-quality silicon-graphene photodetectors, ranging from visual inspection in the lab, to Raman spectroscopy measurements to ensure single-layer, high-quality graphene deposition.

2.1 Overview of Device Architecture

As detailed in Chapter 1, silicon-graphene photodetectors provide a promising path towards high-responsivity, low-power detector solutions. In the following section, the architecture and critical mechanism associated with high internal gain are described in detail. For simplicity, we explain the architecture for a single detector device. However, the operating principle is consistent in the quadrant detectors we also fabricated and discuss in Chapter 4.

2.1.1 High-Gain Silicon-Graphene Detector Architecture

In a graphene-silicon detector design, the semiconductor material works as the light-absorbing medium while the graphene acts as a transparent signal amplifying layer. The exchange

of carriers at the graphene-silicon interface, paired with the high carrier mobility in the graphene, produces an extremely high internal gain.

Devices employing this high-gain mechanism contain four key components: the light-absorbing semiconductor material, an insulating layer, a graphene layer or channel in contact with the semiconductor material, and metal electrodes for signal extraction and device voltage control. As shown in Figure 6 in the device we developed, p-doped silicon is used as the light-absorbing semiconductor material, SiO_2 is used as the insulating layer, the graphene layer (illustrated in black) covers the silicon area where incident light (represented by the red arrow) is absorbed, and Ti/Au electrodes (represented in yellow) are used for the gate (G), source (S), and drain (D) contacts. V_{GS} is the gate/source voltage and V_{DS} is the drain/source voltage, both of which directly control the effectiveness of the high gain system.

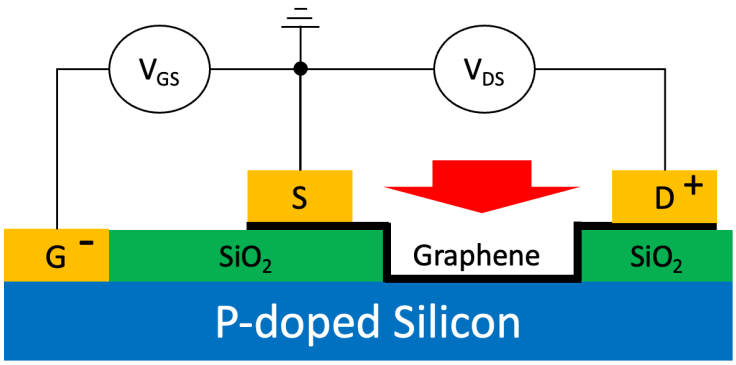


Figure 6. The device we developed uses p-doped silicon (colored in blue) as the light-absorbing semiconductor material and a high-gain graphene channel (colored in black) as the transparent signal amplifying layer.

2.1.2 Silicon-Graphene Device Operating Principle

The fundamental steps of the internal gain mechanism are illustrated in Figure 7. When carriers are generated in the small depletion area at the graphene/silicon heterojunction, the potential imposed in the depletion region (either built-in and/or from applied voltage) rapidly separates an electron and hole pair, such that they cannot immediately recombine. In the case of a

p-doped silicon substrate, the electron is injected into the graphene, and the coupled hole remains trapped in the silicon for an extended period, before recombination occurs.

Once an electron (the carrier) is injected into the graphene, it travels at extremely high velocity, allowing it to move to the drain electrode and be replaced multiple times by other electrons from the source electrode. Once the hole in the silicon recombines with an electron in the silicon, the electron in the graphene is no longer coupled and therefore it transitions to the drain electrode without replacement. The theoretical gain from this mechanism is directly proportional to the number of times the electron in the graphene is replaced before recombination occurs.

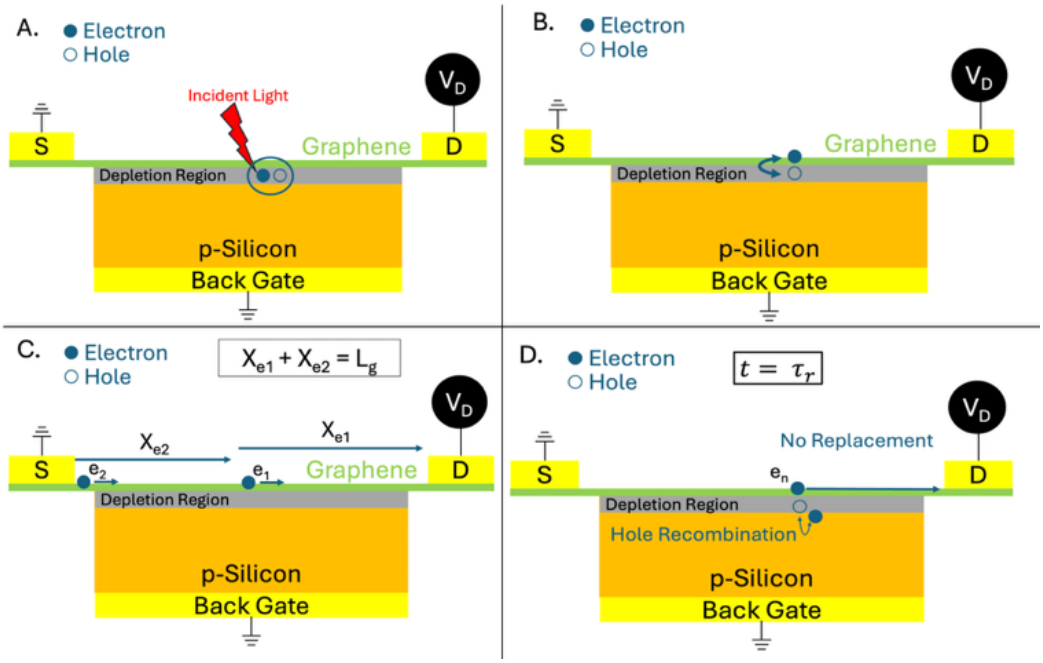


Figure 7. Illustration of the quantum gain, or Quantum Carrier Reinvestment mechanism. **(A)** Incident photons indicated by the red arrow generate electron hole pairs in the depletion region. **(B)** The imposed potential rapidly separates the carriers and injects electrons into the graphene channel. These carriers are coupled until the corresponding coupled holes in the silicon recombine. **(C)** The electron moves extremely rapidly in the graphene, where it takes time $t = \tau_t$ for them to travel from one electrode to the other, allowing the carrier to be replaced multiple times by another electron from the source contact in a short time. The original electron, e_1, moves a distance X_{e1} to the drain contact and is replaced by electron e_2 that travels a distance X_{e2} from the source contact, resulting in an effective movement of one electron from source to drain. This occurs many times while the electron's position is coupled to the hole in the silicon. **(D)** Once the hole in the silicon recombines at $t = \tau_r$, the electron in the graphene is no longer coupled to the position and moves to the drain contact, ending the gain process.

As proposed by Liu and Kar in their Quantum Carrier Reinvestment mechanism [1], the gain can be partially modeled using the photoconductive gain (G_P)

$$G_P \equiv \frac{\tau_r}{\tau_t} = \frac{\tau_r \mu V_{DS}}{{L_g}^2}, \tag{2.1}$$

where τ_r is the recombination time of the device, τ_t is the transit time between the source and drain electrodes, μ is the carrier mobility in graphene, V_{DS} is the applied source-drain voltage, and L_g is the distance between the source and drain electrodes (i.e., the graphene channel length).

Equation 2.1 captures the quantum gain effect but fails to accurately account for the mechanism's dependence on incident power (P), causing mismatches between the theoretical predictions and the experimental data [1, 2, 3]. For example, Liu and Kar propose a responsivity slope proportional to ~$P^{-0.38}$ but the experimental responsivity slope is proportional to ~$P^{-0.83}$ [1]. Additional effects in the junction that are difficult to separate, such as variations in graphene's mobility and the quantum capacitance, both being a function of incident power, contribute to this mismatch.

Nonetheless, the responsivity depends on incident power (typically ~$P^{-0.8}$ [1, 2]) and environmental factors, making it difficult to maintain stability of operation, especially when using traditional transimpedance readout schemes [4]. Taking these factors in consideration, we developed an electronic feedback system that provides stabilization and produces a far more stable response over a broad range of incident power and temperature. This novel stabilization mechanism is described in Chapter 3.

2.2 Overview of Device Fabrication Process

The device we developed was fabricated at the University of Michigan Lurie Nanofabrication Facility (LNF) utilizing standard silicon manufacturing processes. Below we detail the fabrication steps taken to produce silicon-graphene photodetectors. It is important to note

that the fabrication steps taken for both single detectors and quadrants detectors are nearly identical – the only difference being the design of the photolithography masks.

2.2.1 Device Design Preparation & Lithography Mask Etching

Each device was designed using *kLayout*, a layout editor widely used for nanofabrication. The device geometry was designed layer-by-layer, with each layer corresponding to a critical lithography step in the fabrication process, such as the oxide etching, graphene patterning, or electrode deposition. Each layer corresponds to the need for a lithography mask, and thus, three masks were made for our detector designs: (1) a mask for the SiO_2 etching to expose light-absorbing Si windows, (2) a mask for graphene patterning, and (3) a mask for electrode metal deposition. Moreover, precise alignment marks were added to each mask to enable layer alignment throughout the fabrication process of the device.

Following layout design, each of the three photolithography masks were fabricated. These masks were generated using the Heidelberg μPG 501 mask writer, which exposes a photoresist-coated chromium mask according to the patterns defined in the KLayout design files. After exposure, the masks were developed to remove the exposed photoresist, revealing the underlying chromium in the patterned regions.

The exposed chromium was then selectively etched, transferring the design pattern into the chromium layer and forming a durable photomask. The remaining photoresist was subsequently stripped, leaving a clean chromium-on-glass mask. Each mask was inspected under an optical microscope to verify pattern fidelity, edge definition, and cleanliness prior to use in device fabrication.

2.2.2 Silicon Wafer Etching & Dicing

Commercially available p-doped silicon substrates with a resistivity of 10–20 Ω-cm and a 100 nm thermally grown SiO_2 layer were procured and used as the base of our detectors. Lightly p-doped silicon was selected to address a gap in the literature, where prior silicon-graphene photodetector studies have predominantly focused on lightly n-doped silicon, while the 100 nm SiO_2 layer was chosen as the thinnest commercially available oxide that still provided complete electrical isolation between the later-deposited electrodes and the bulk silicon.

As a first step, the thermal oxide needed to be etched in the desired device active areas, exposing the light-absorbing p-doped silicon. To do so, we used the TEL Mark Vz Coater to deposit approximately 3µm of SPR 220 photoresist. Hexamethyldisilazane (HMDS) was used to promote adhesion of the SPR 220 photoresist to the wafer, and a 90 second softbake at 115°C was used to solidify the deposited photoresist. Next, the GCA AS200 Autostep was used to enable submicron precision projection lithography. Using the previously prepared lithography masks, the device active areas were patterned along the wafer surface. An optimized exposure time of 0.32s was used for this step to ensure sharp features. A 90 second post-exposure bake at 115°C was then performed to promote photoresist crosslinking and improve feature definition. Following this, the exposed wafer was developed using either the TEL Mark Vz system or the CEE developer. After development, the sample was inspected under an optical microscope to verify complete removal of the exposed photoresist and ensure that well-defined features were obtained. In cases where residual photoresist patterns such as streaks or swirls were observed, a short additional development step was performed to fully clear the patterned regions.

To remove any remaining photoresist residue and improve pattern fidelity, a descum step was carried out using an oxygen plasma in the YES Plasma system for 20 seconds. The wafer was

then subjected to a buffered hydrofluoric acid (BHF) etch for approximately 1 minute to selectively remove the exposed SiO_2 and reveal the underlying p-doped silicon in the active device regions. Following the etch, the sample was thoroughly rinsed and inspected to confirm strong contrast between the remaining SiO_2 and the exposed silicon, indicating successful oxide removal.

Finally, the remaining photoresist was stripped using a 14-minute soak in Nanostrip. A final inspection was performed to ensure complete removal of the photoresist and to verify that the etched features were clean and well-defined. This process resulted in precisely patterned openings in the SiO_2 layer, defining the active regions for subsequent graphene integration and device fabrication. A wafer with exposed Si regions is shown in Figure 8.

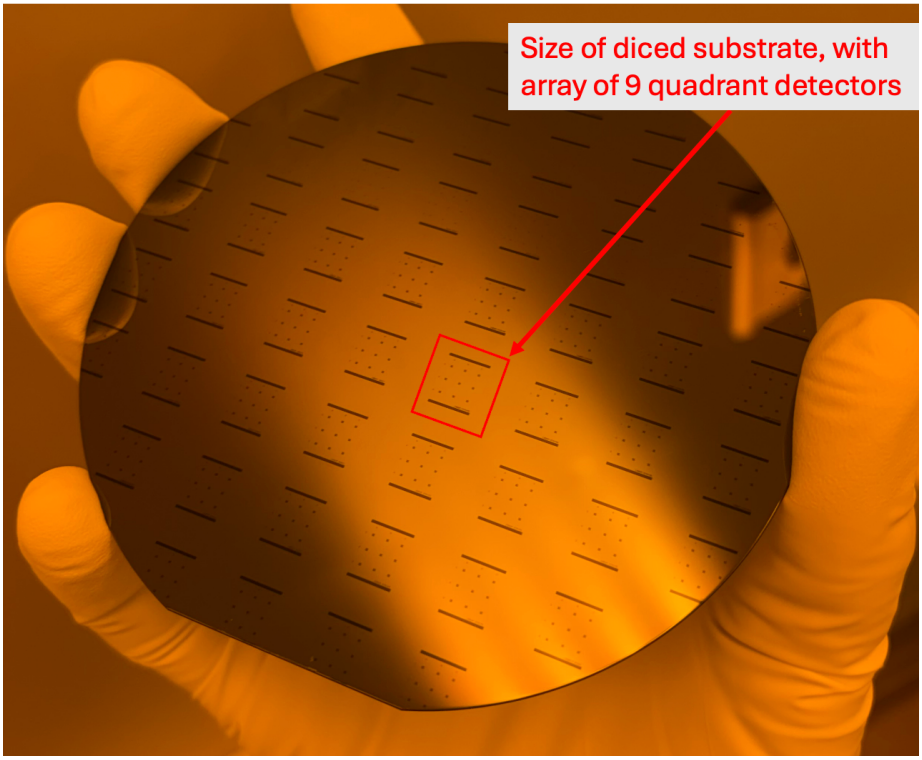


Figure 8. Silicon/SiO_2 wafer following selective SiO_2 etching used to define photodetector geometries. The device array is deliberately spaced to facilitate wafer cleaving into smaller dies for subsequent processing and integration steps.

Following the oxide etch and photoresist removal, the wafer was diced into individual samples using a manual scribing process. A tungsten-carbide scribe was used to create a controlled

scratch along the ⟨110⟩ crystallographic direction of the silicon wafer, which corresponds to a preferred cleavage plane. After scribing, gentle mechanical force was applied to cleave the wafer along the defined line, resulting in cleanly separated individual dies. This method enabled precise and low-cost sample preparation for subsequent processing and characterization steps.

2.2.3 Graphene Deposition

Following the definition of the active device regions, graphene was integrated onto the patterned substrates using a wet transfer process. In this work, commercially available Trivial Transfer® graphene provided by ACS Material was utilized. This material consists of a high-quality single-layer graphene film supported by a polymethyl methacrylate (PMMA) layer, enabling straightforward transfer onto arbitrary substrates without the need for specialized equipment. The transfer process leverages the hydrophobic nature of the polymer-supported graphene, allowing it to be manipulated and deposited using deionized (DI) water and standard laboratory tools such as tweezers. The deposition process flow and a photo showing the graphene immersion into DI water is shown in Figure 9.

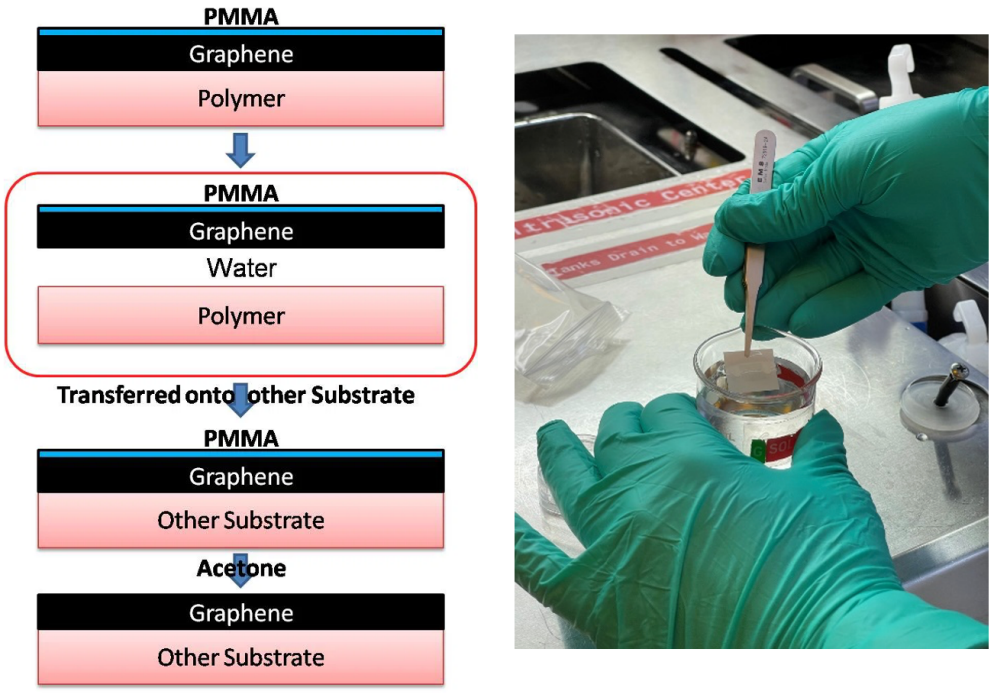


Figure 9. (**Left**) Process flow illustrating the transfer procedure for Trivial Transfer graphene obtained from ACS. Reproduced from ACS Material. (**Right**) Photograph of the graphene sheet immersed in deionized (DI) water at the solvent bench prior to transfer onto the target device substrate.

To initiate the transfer, the edges of the graphene-polymer film were first wetted with high-purity DI water and allowed to sit for approximately 3 minutes to facilitate separation from the backing substrate. The sample was then immersed in a DI water bath for 2 hours to fully release the graphene-polymer film. Following this initial soak, the film was sequentially transferred through two additional high-purity DI water baths for 1 minute each to remove residual contaminants and improve film cleanliness.

After rinsing, the graphene-polymer film was transferred onto the pre-patterned silicon substrate by gently bringing the substrate into contact with the floating film. The sample was then held vertically for approximately 2 minutes to allow excess water to drain, promoting uniform adhesion of the graphene layer to the substrate. The sample was subsequently allowed to air-dry

for 30 minutes to further stabilize the transferred film. Images of successful and unsuccessful graphene-polymer film depositions onto a diced substrate are shown in Figure 10.

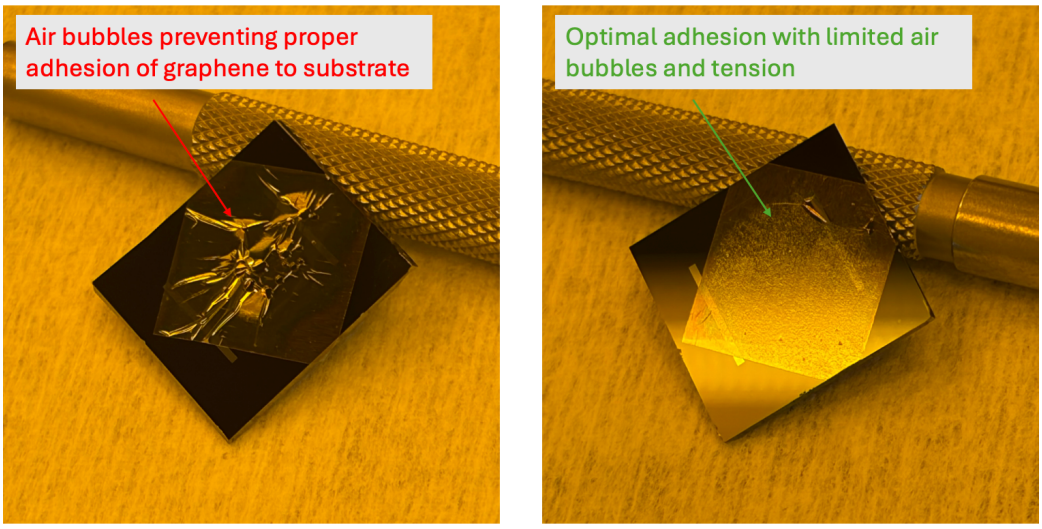


Figure 10. Images of graphene-PMMA wet transfer results onto the detector surface. (**Left**) Unsuccessful transfer showing significant air bubble formation and folding of the graphene-PMMA film across the active detector region, which can degrade device performance and film continuity. (**Right**) Successful transfer exhibiting good film uniformity across the graphene-PMMA sheet with minimal trapped air bubbles and improved coverage of the detector area.

To improve adhesion and remove residual moisture, the sample was baked at 100°C for 20 minutes. During this time, an acetone bath was heated to approximately 50°C in preparation for polymer removal. Following the bake step, the sample was immersed in the heated acetone bath for 30 minutes to dissolve the PMMA support layer, leaving behind the transferred graphene film. The sample was then removed from the acetone bath, gently dried using a nitrogen gun, and subjected to a final bake at 45°C for 20 minutes to eliminate residual solvent and ensure a clean, well-adhered graphene layer, as shown in Figure 11.

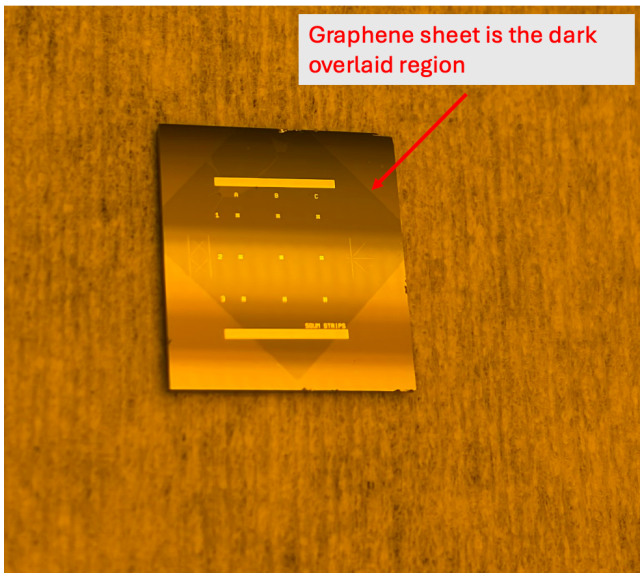


Figure 11. Image of the device following acetone soaking and PMMA removal, leaving behind the transferred graphene layer on the detector surface. The graphene film demonstrates good uniformity and consistent coverage across the detector regions, indicating a successful transfer and cleaning process.

This transfer process results in a conformal graphene film deposited directly onto the exposed silicon regions, forming the basis for subsequent device patterning and electrical integration.

2.2.4 Graphene Patterning & Etching

Following graphene transfer, the graphene layer was patterned to define the active device geometries using standard photolithography and dry etching techniques. A layer of SPR 220-3.0 photoresist was first spin-coated onto the graphene-coated samples using the CEE 200X photoresist spinner at 3000 RPM, resulting in an approximately 3 μm thick resist layer. The coated samples were then soft-baked at 115°C for 90 seconds to remove residual solvents and improve resist adhesion.

The patterned photoresist was defined using projection lithography on the GCA AS200 AutoStep system. An exposure time of 0.32 seconds was used to ensure well-defined features, and alignment marks were set to negative to match the mask design. Care was taken to ensure proper

sample orientation during alignment, with alignment indicators positioned appropriately to maintain consistency across exposures. Following exposure, the samples were removed from the system for post-processing.

A post-exposure bake was performed at 115°C for 90 seconds to enhance resist profile definition. The samples were then developed using the CEE developer with the AZ726 40-40 developer recipe optimized for small samples. After development, the samples were inspected under an optical microscope to verify complete removal of exposed resist regions and to ensure accurate pattern transfer. If residual photoresist features such as streaks or incomplete development were observed, a short additional development step was performed.

Graphene in the exposed regions was removed using oxygen plasma etching in the Plasmatherm 790 system. A standard descum recipe was used for 3 minutes to ensure complete removal of graphene in the unprotected regions. The remaining photoresist was subsequently removed by soaking the samples in acetone or Remover PG overnight, ensuring complete resist lift-off without damaging the patterned graphene.

Finally, the samples were inspected to confirm that the graphene had been cleanly and accurately patterned, with well-defined edges and minimal residual contamination. This process resulted in precisely defined graphene features aligned to the underlying silicon device regions, enabling subsequent metallization and device integration. Patterned graphene areas for our single detector and quadrant detector devices are shown in Figure 12.

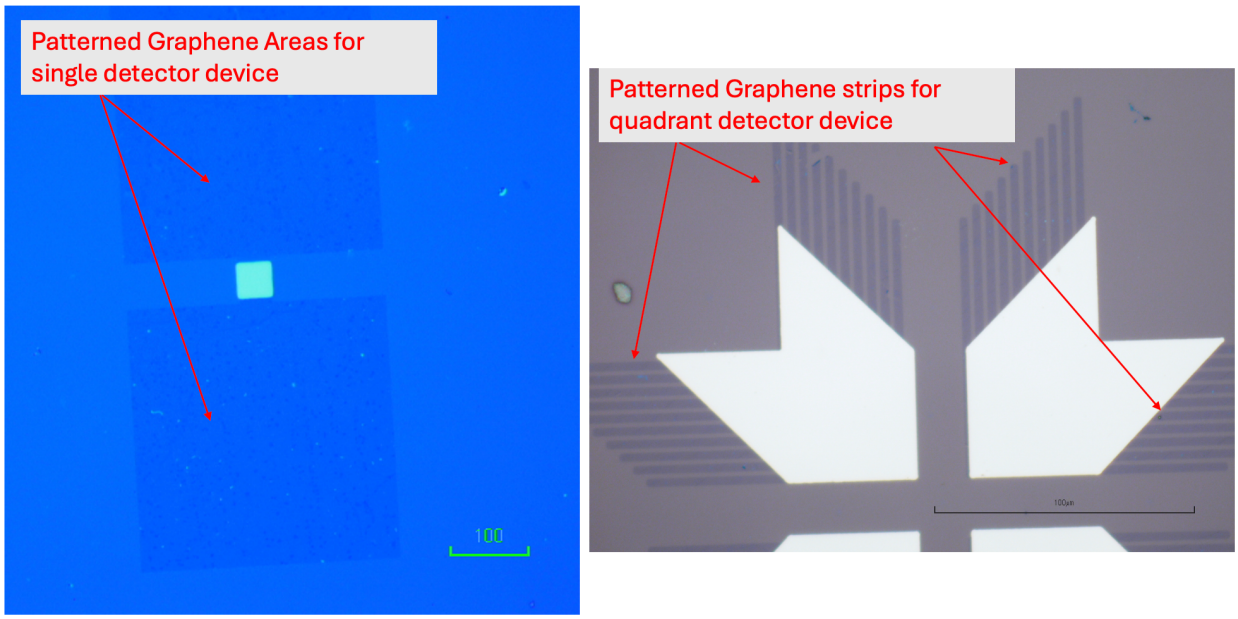


Figure 12. (**Left**) Single-element detector device we fabricated showing patterned graphene in the electrode regions prior to metal deposition. The graphene transferred over the light blue silicon (Si) window is not visible due to its optical transparency. (**Right**) Fabricated quad-cell detector featuring graphene strips transferred across the light-colored arrow-shaped Si windows for photodetection operation.

2.2.5 Metal Electrode Patterning & Deposition

Following graphene patterning, metal electrodes were defined to enable electrical contact to the graphene and underlying silicon regions. A layer of SPR 220-3.0 photoresist was first spin-coated onto the samples using the CEE 200X photoresist spinner at 3000 RPM, resulting in an approximately 3 µm thick resist layer. The samples were then soft-baked at 115°C for 90 seconds to remove residual solvents and improve resist adhesion.

Photolithographic patterning of the electrode structures was carried out using the GCA AS200 AutoStep system with an exposure time of 0.32 seconds to achieve well-defined electrode features. Careful alignment was performed to ensure that the metal electrodes were accurately positioned relative to the graphene active regions. Following exposure, the samples were removed from the system and subjected to a post-exposure bake at 115°C for 90 seconds.

The exposed samples were then developed using the CEE developer with the AZ726 40-40 developer recipe optimized for small samples. After development, the samples were inspected under an optical microscope to verify complete removal of exposed resist and to ensure accurate pattern transfer. A short additional development step was performed if incomplete development or residual photoresist artifacts were observed.

Metal electrodes were deposited using the Enerjet electron-beam evaporator. A bilayer metal stack was employed, consisting of a 20 nm titanium (Ti) adhesion layer followed by a 250 nm gold (Au) layer. The specific electrode thickness was chosen to provide a robust foundation for wire bonding. The Ti layer was deposited at a rate of approximately 10 Å/s to promote strong adhesion between the gold and the underlying graphene and silicon surfaces. Subsequently, the Au layer was deposited at a rate of approximately 8 Å/s to form low-resistance electrical contacts and robust bonding pads.

Following metal deposition, the samples were subjected to a lift-off process to remove unwanted metal and define the final electrode geometry. The samples were soaked in acetone or Remover PG overnight to dissolve the underlying photoresist layer. After soaking, any remaining metal was gently removed using an acetone rinse, allowing excess gold to lift off cleanly from the surface. Finally, the samples were inspected to ensure that the metal electrodes were well-defined, properly aligned, and free of defects such as flaking or incomplete lift-off. An image of a successful metal electrode deposition is shown in Figure 13.

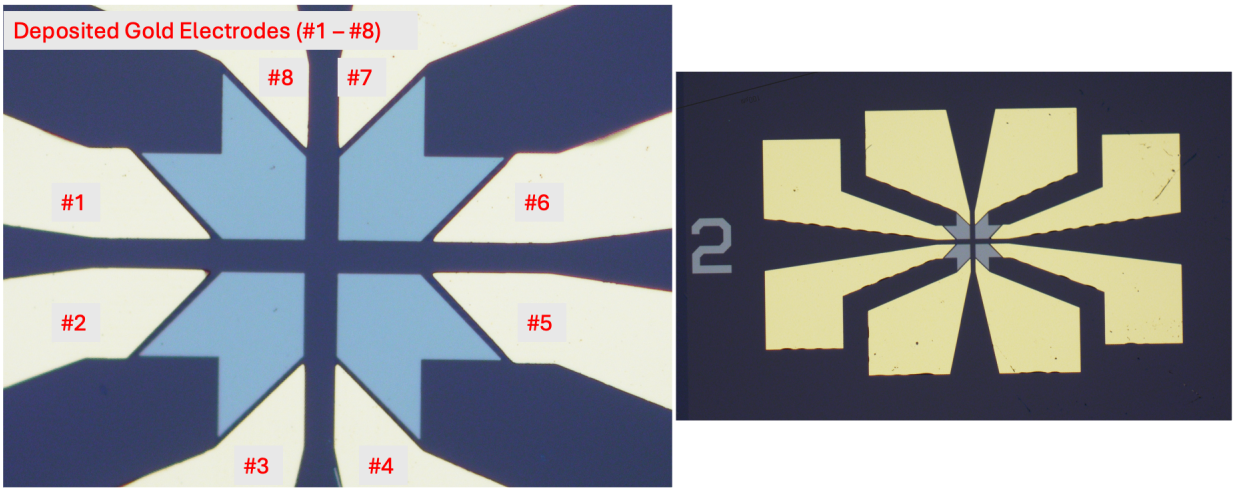


Figure 13. (**Left**) Microscope image of the fabricated quad-cell detector following metal electrode patterning and deposition. The electrodes are accurately aligned around the detector active regions and are designed with sufficient pad area to support subsequent wire bonding operations. (**Right**) Photograph of the fully fabricated detector prepared for the next fabrication stage, packaging and integration.

2.2.6 Device Packaging

Once metal electrodes were defined on the samples, the substrate housing the detectors was fixed to a leadless chip carrier using Kapton tape. This prepared the sample for wire bonding, where thin gold bonds would connect device electrodes to the surrounding leadless chip carrier electrodes. The MPP iBond 5000 Ball Bonder was used for this, and the appropriate recipe was optimized for our devices. Careful selection of the work holder temperature, binding force, wire loop, and bonding time ensured strong and reliable bonds between detectors and the chip carrier. Moreover, the gate contacts (large bars at the top and bottom of the sample) were also wire bonded to provide a way of tuning the gate voltage of the device.

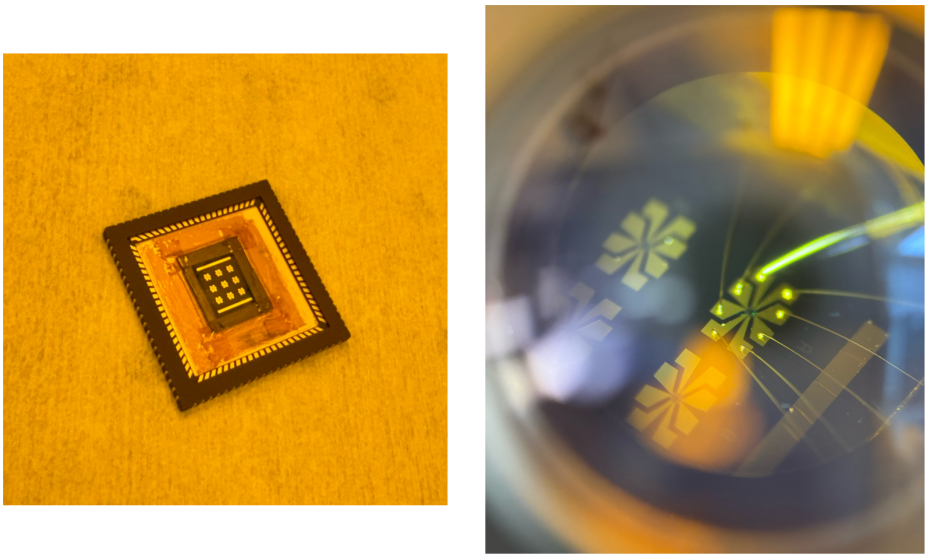


Figure 14. (**Left**) Completed device mounted in a leadless chip carrier (LCC) and secured using Kapton tape for stable electrical interfacing during testing. (**Right**) Optical microscope image showing wire bonds connecting the contact pads to the quadrant photodetector, enabling independent electrical access to each quadrant.

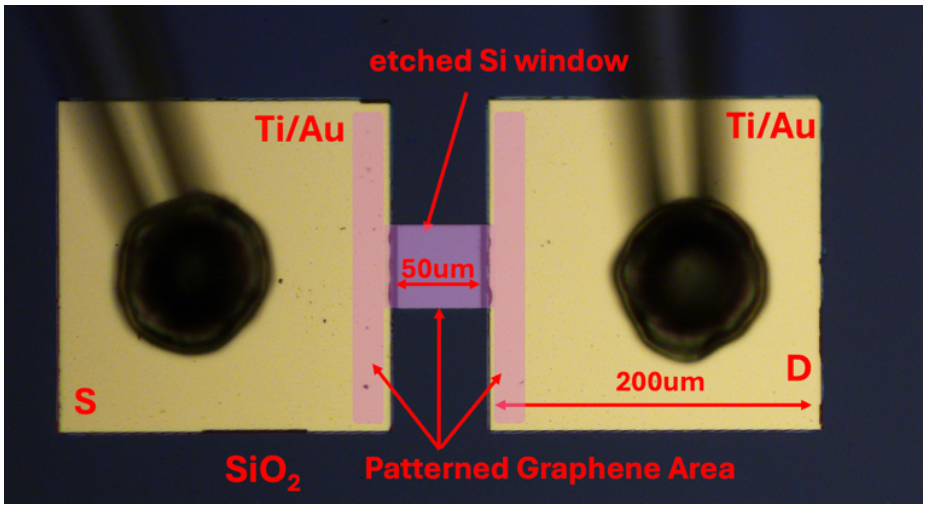


Figure 15. Microscope image of a prototype wire bonded single silicon-graphene detector. The patterned graphene area (purple) was designed to maximize the contact area between the graphene and the source/drain electrodes. The gate contact is not shown here.

2.3 Device Quality & Operation Verification

To produce high quality devices, various quality-control steps were taken during and after the fabrication process. These steps included visual inspections of the device between fabrication

process steps, Raman spectroscopy measurements of the deposited graphene, and electrical testing of the devices to ensure their functionality.

2.3.1 Visual Inspection of Devices

Throughout the fabrication process, critical checkpoints were established at which visual inspection was performed to ensure process fidelity. These inspections were conducted after key steps, including photoresist exposure and development, lift-off, and all etching processes. Optical microscopy was used to evaluate device features, with particular attention to incomplete or non-uniform photoresist development, interlayer misalignment, and residual contamination from prior steps.

Implementing these inspection stages was essential for maintaining high fabrication quality, as they enabled early detection of errors before subsequent, irreversible steps were performed. For instance, an incorrectly oriented photolithography step could be identified immediately after development, allowing the photoresist to be stripped and the patterning process repeated. Additionally, underdeveloped photoresist (shown in Figure 16) was also rapidly identified and addressed by running an additional development cycle.

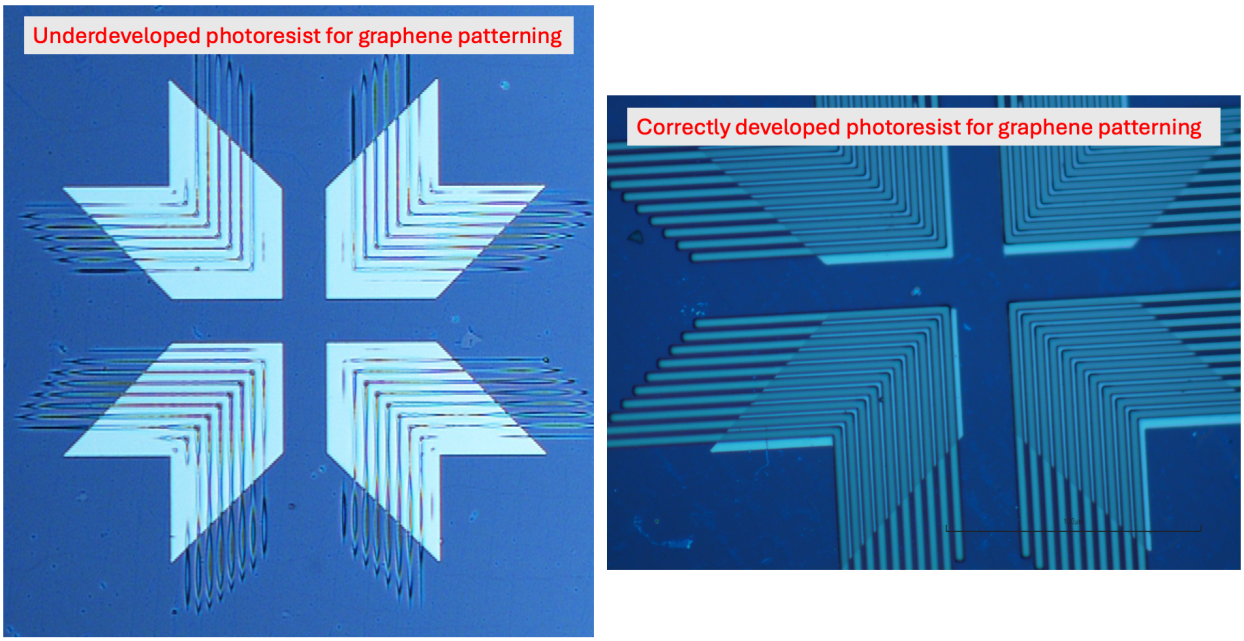


Figure 16. (**Left**) Example of improperly developed graphene fingers following lithography, identified by rainbow-colored streaking, residual photoresist, and poorly defined feature edges. (**Right**) Correctly developed sample exhibiting sharp graphene finger features and uniform pattern definition.

In addition to preventing critical failures, these inspections ensured well-defined, high-resolution feature edges throughout the fabrication sequence. The sharpness of feature edges is critical for high-quality devices, and ensuring consistency throughout the fabrication process helped build confidence in the tool parameters we were using. The result of these extensive and progressive checkpoints resulted in a significant improvement of detector yield over four sequentially fabricated samples (Figure 17).

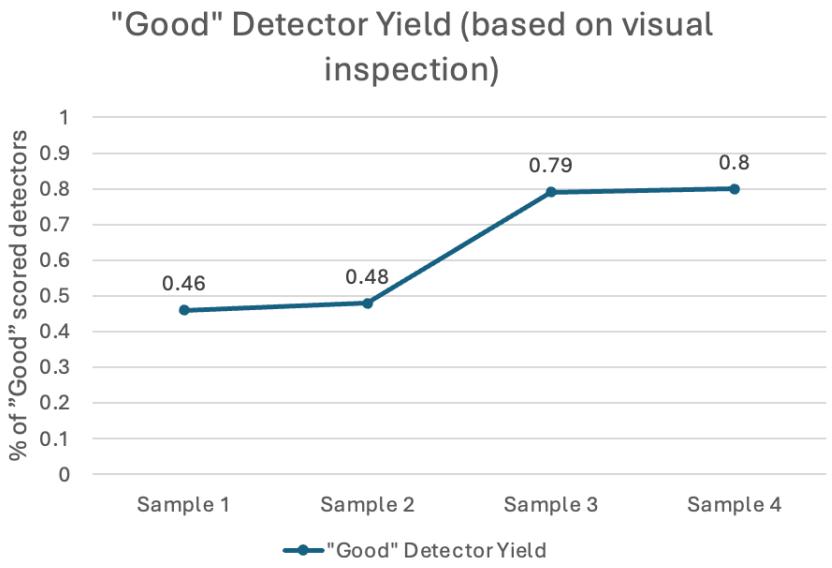


Figure 17. Detector yield across four fabricated samples, each containing multiple individual detectors. A detector was classified as "good" if no visible defects were observed during post-fabrication inspection. All detectors categorized as "good" were subsequently electrically tested and confirmed to be operational. The results demonstrate a progressive improvement in fabrication yield across successive samples.

2.3.2 Raman Spectroscopy Analysis of Deposited Graphene

Verification of high-quality graphene in the detector region was fundamental to ensuring a robust fabrication process. To ensure this, Raman spectroscopy measurements were done in graphene-populated regions on Si and on SiO_2. Measurements taken on one of the better-performing detectors is shown in Figure 18.

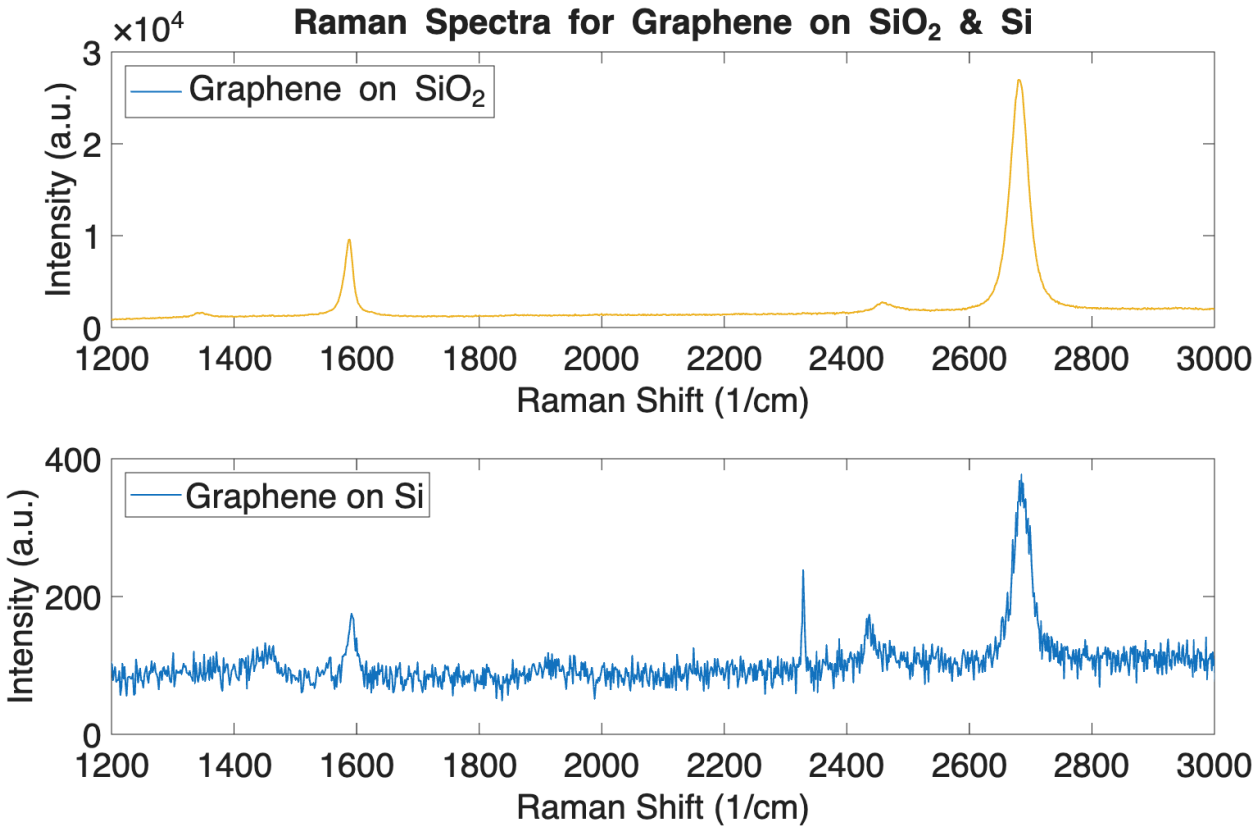


Figure 18. Raman spectra of transferred graphene measured on SiO_2 (top) and Si (bottom) substrates. Distinct graphene G and 2D peaks are observed near ~1580 cm^{-1} and ~2680 cm^{-1}, respectively, confirming the presence of graphene following transfer. Differences in peak intensity between the two spectra arise from substrate-dependent effects.

Strong G and 2D peaks were observed, indicating the presence of single layer of graphene in the silicon window region and on the SiO_2 region prior to the electrodes. The decreased intensity of the peaks in the Si region is likely due to the substrate effect, as mentioned in Liu and Kar (2014) [1].

2.3.3 Minority Lifetime Measurements & Back Gate Current Measurements

Once the detectors were packaged and wire bonded, a series of electrical and optical characterization tests were conducted to verify device operability and evaluate performance. Initial electrical testing involved applying a bias across the source and drain electrodes to confirm current transport through the graphene channel. Following this initial verification, two additional

measurements were performed: minority carrier lifetime testing and back-gate current testing. Minority carrier lifetime testing was conducted because the carrier lifetime is directly related to the expected photoconductive gain and response time of the detector. For this measurement, an optical chopper was added to the experimental setup to modulate the incident light source, and the resulting time-dependent signal response was recorded. The minority carrier lifetime was then extrapolated from the decay of the measured signal, with the results shown in Figure 19. These results are consistent with typical lightly p-doped silicon recombination times for the given optical injection [6].

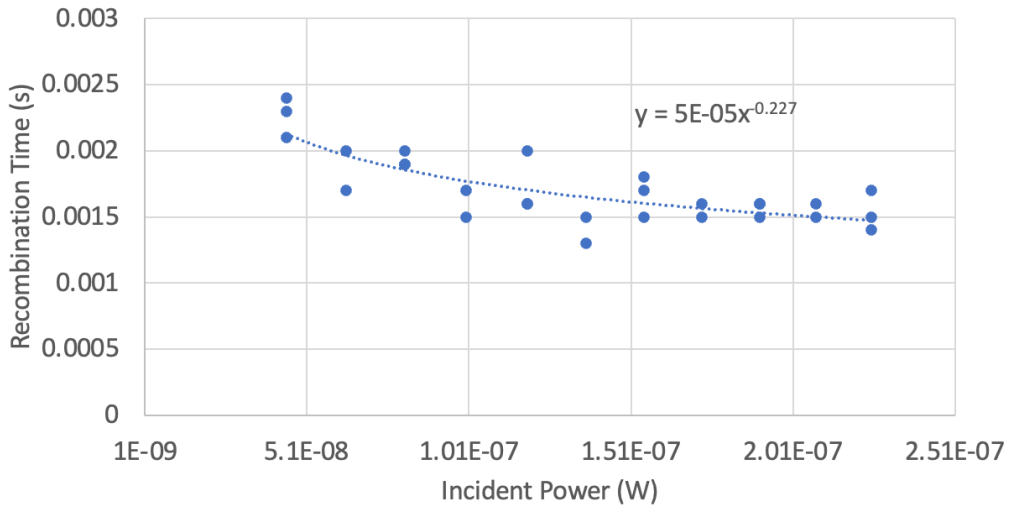


Figure 19. Recombination time as a function of incident optical power. The recombination time was extracted from the decay of the detector signal following optical modulation at each incident power level. The measured trend shows how carrier recombination dynamics vary with illumination intensity, providing insight into the minority carrier lifetime and its influence on detector gain and response time.

Back-gate current testing was then performed to verify whether photogenerated carriers were being injected from the silicon substrate into the graphene channel, which is the proposed mechanism responsible for the induced gain. In this test, a bias was applied between the source/drain electrodes and the back gate, and the resulting current response was measured. The measured behavior shown in Figure 20 followed the characteristic response of a diode, confirming

that carriers transition between the bulk silicon and graphene. These results validate the operating principle of the gain mechanism introduced in this detector architecture.

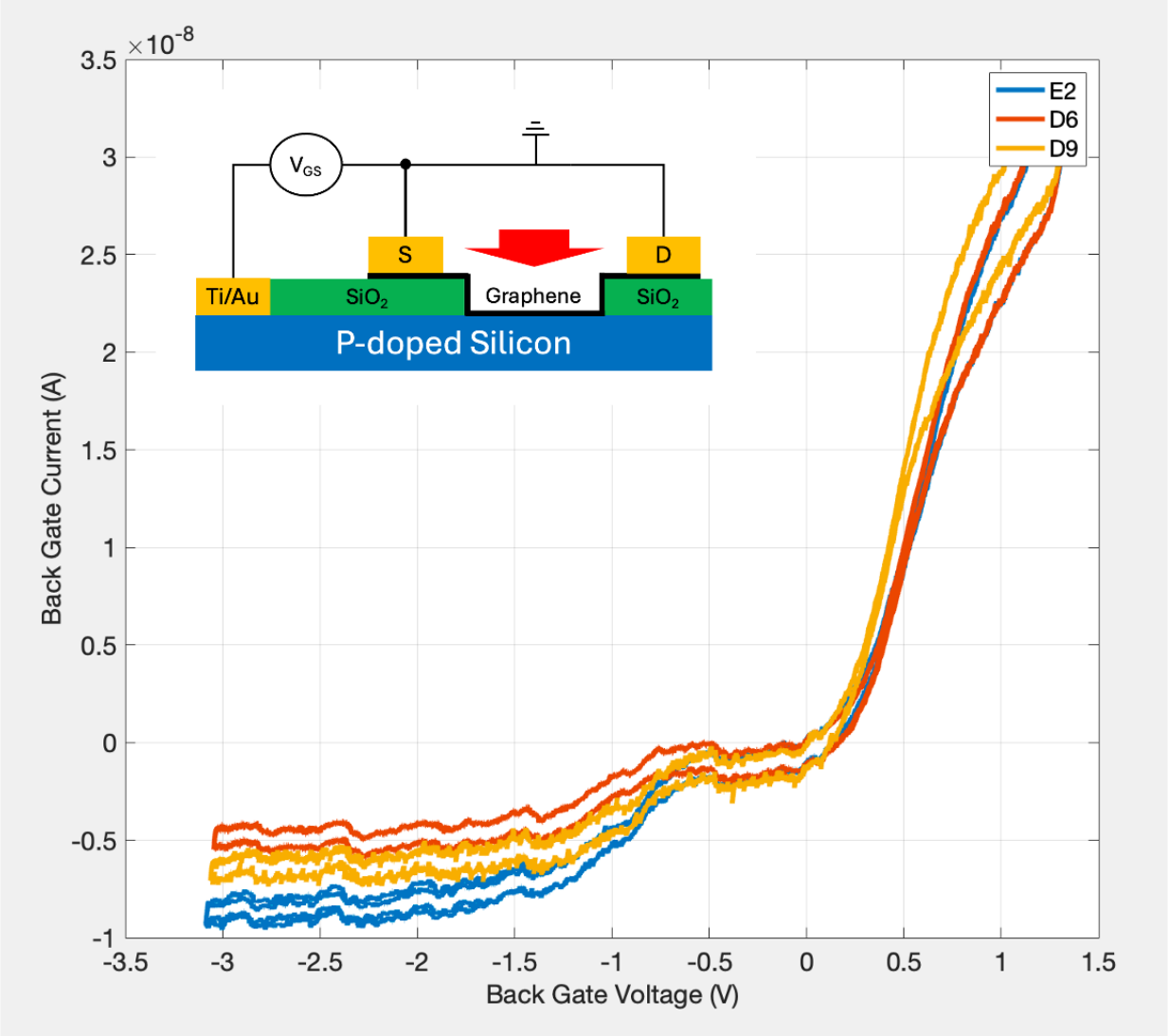


Figure 20. Back-gate current measurements for representative silicon-graphene detectors. The measured response follows diode-like behavior, indicating that carriers are injected across the silicon-graphene interface and supporting the proposed gain mechanism. Detectors E2, D6, and D9 are labeled according to their row and column positions on the fabricated detector sample.

2.3.4 High-Gain & Enhanced Responsivity Verification

Following back gate and lifetime testing, photoresponse measurements were performed using a focused low-power 635 nm laser while the device was under bias to evaluate photoconductive gain and responsivity enhancement. The incident laser was modulated, and the

resulting responsivity was calculated and compared against previously reported values in the literature. An example of the detector response is shown in Figure 21.

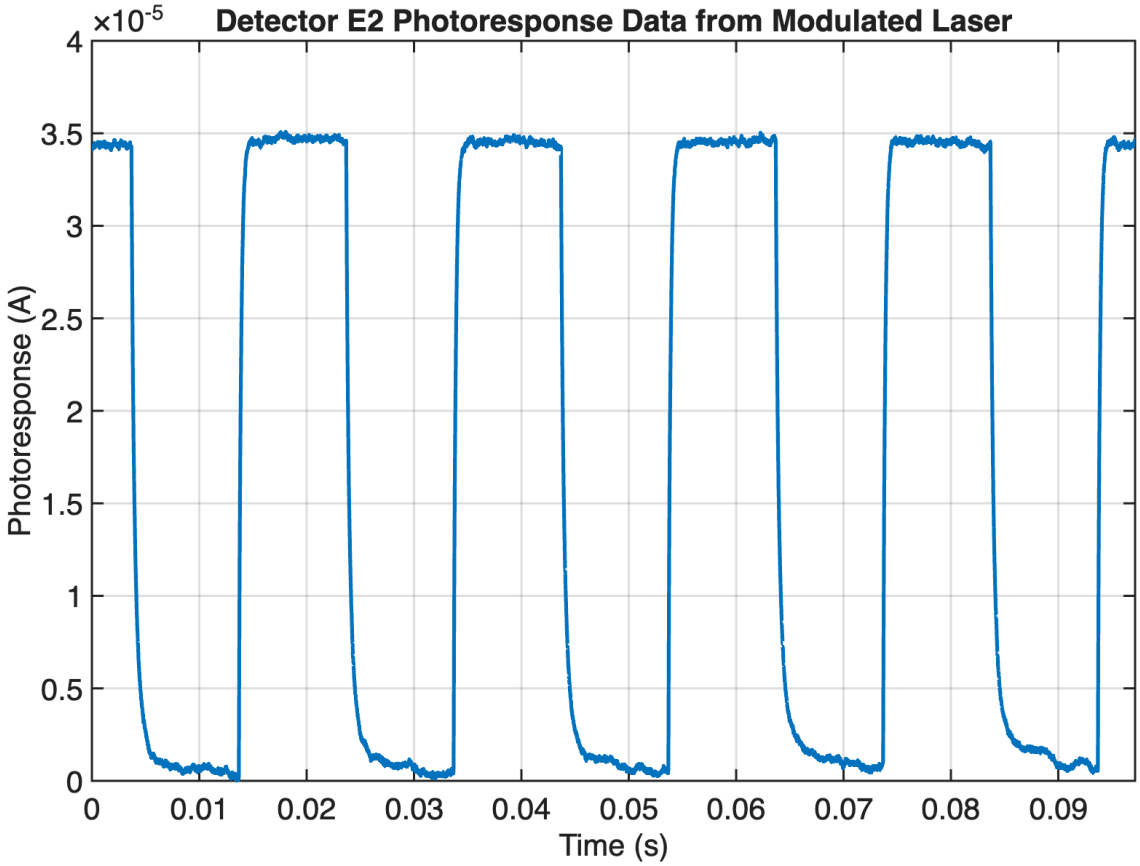


Figure 21. Time-domain photoresponse of detector E2 under illumination from a modulated laser source. The measured transimpedance amplifier output voltage was converted to photocurrent using the 2 kΩ feedback resistor. The photocurrent was subsequently zeroed by subtracting the initial measured value, and the response is plotted as a function of time with the initial measurement point shifted to t=0 s. The incident laser was modulated between approximately 45 nW and 225 nW optical power, producing the periodic photocurrent variations observed in the signal. The detector clearly resolves the optical modulation, demonstrating its ability to detect low-flux, time-varying optical signals.

For multiple samples fabricated, identified according to their row-number and column-letter location on the substrate, responsivity was measured as a function of incident optical power. Within the power regime tested, many devices demonstrated performance exceeding previously reported graphene-silicon photodetectors, exhibiting both higher responsivity and a stronger increase in responsivity as incident power decreased. The responsivity of the devices is calculated using the difference between the detector signal with and without incident light, divided by the

incident power on the detector. As shown in Figure 22, detectors illuminated with 785 nm light at an incident power of 1 μW achieved responsivities approaching >300 A/W, exceeding the native silicon responsivity of approximately 0.5 A/W by nearly three orders of magnitude at the same wavelength. The results presented also highlight the non-linear nature of these detectors and enhanced performance at low incident powers. Furthermore, Figure 23 presents the detector performance extrapolated to lower incident powers, suggesting that responsivities at the 1 pW level may reach values approximately two to three orders of magnitude greater than those reported in the literature under similar operating conditions and of identical size [1]. We show this extrapolation to low incident powers because the literature suggests that this detector technology can operate in this regime. However, experimental verification is necessary and would require a carefully controlled low-light environment with a low-noise lock-in amplifier.

These results verified not only that the detectors we fabricated were fully operational, but also that the fabrication process consistently produced high-quality, high-performance devices. The performance and fabrication repeatability of the devices we fabricated established a strong foundation for the development and characterization of the novel stabilization mechanism presented in Chapter 3.

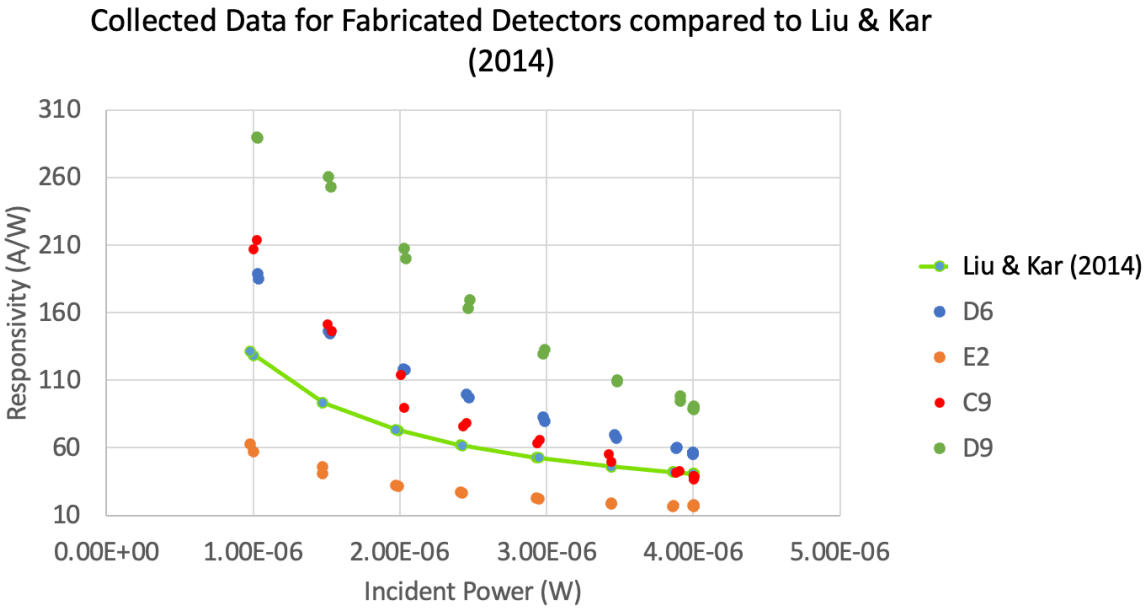


Figure 22. Responsivity as a function of incident optical power for multiple fabricated silicon-graphene photodetectors under 785 nm laser illumination, compared with the results of Liu and Kar (2014). Detectors are identified by their row-number and column-letter position on the substrate. Measured devices exhibited higher responsivity and a steeper increase in responsivity at lower incident powers compared to the literature.

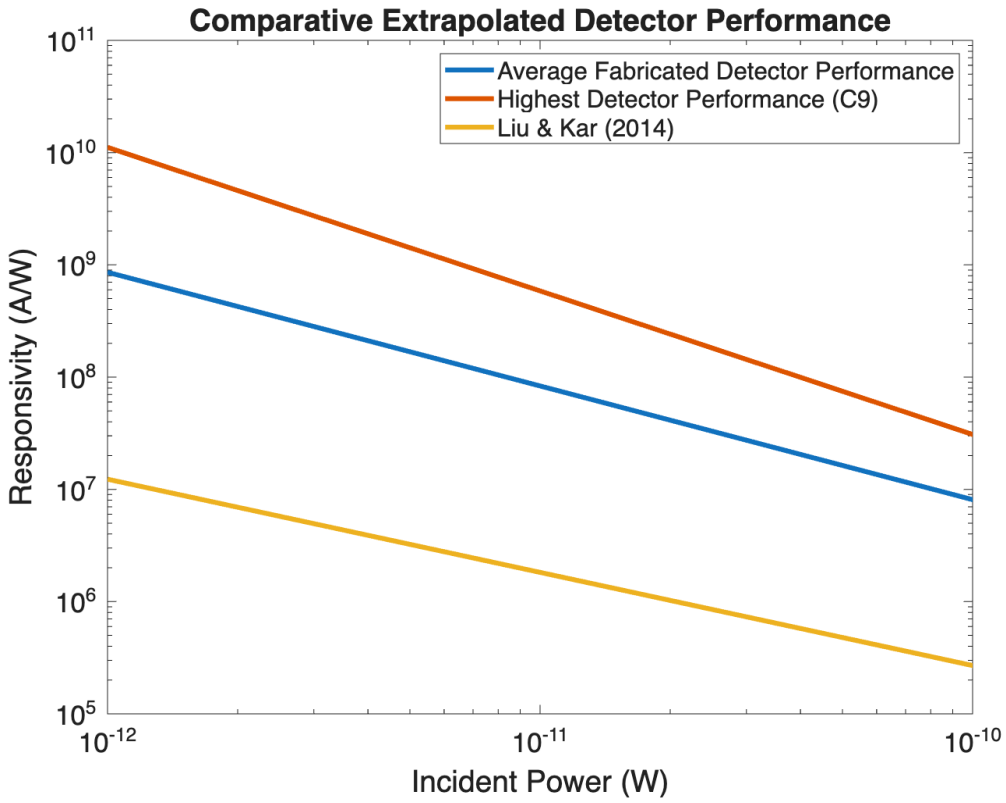


Figure 23. Extrapolated responsivity trends showing the average performance of all operational detectors, the highest-performing detector, and the results from Liu and Kar (2014). The extrapolation suggests responsivities up to 2–3 orders of magnitude greater than previously reported values at picowatt-level incident powers.

2.4 References

[1] Liu F, Kar S. Quantum Carrier Reinvestment-induced ultrahigh and broadband photocurrent responses in graphene-silicon junctions. ACS Nano. 2014 Oct 28;8(10):10270-9. doi: 10.1021/nn503484s. Epub 2014 Oct 17. PMID: 25325405.

[2] Iqbal, S., Imran, H., Qasim, U. B., & Butt, N. Z. (2017). Design of high performance graphene/Silicon photodetectors. *2017 International Conference on Simulation of Semiconductor Processes and Devices (SISPAD)*, 205–208. https://doi.org/10.23919/sispad.2017.8085300

[3] Butt, Nauman Z., et al. "Substrate-Induced Photofield Effect in Graphene Phototransistors." *IEEE Transactions on Electron Devices*, vol. 62, no. 11, Nov. 2015, pp. 3734–41. *DOI.org (Crossref)*, https://doi.org/10.1109/TED.2015.2475643.

[4] Meca Meca, F.J.; Martín-Gorostiza, E.; García-Garrido, M.Á.; Salido-Monzú, D. Phase Stability under Thermal Drifts in Photodiode-Conditioning Transimpedance Amplifiers for Distance Metrology. *Sensors***2021**, *21*, 3455. https://doi.org/10.3390/s21103455

[5] Ferrari, A., Basko, D. Raman spectroscopy as a versatile tool for studying the properties of graphene, *Nature Nanotech* **8**, 235–246 (2013). https://doi.org/10.1038/nnano.2013.46

[6] R. A. Sinton and R. M. Swanson, "Recombination in highly injected silicon," *IEEE Transactions on Electron Devices*, vol. 34, no. 6, pp. 1380–1389, Jun. 1987. doi:10.1109/t-ed.1987.23095

Chapter 3 Low-Noise Stabilization Mechanism to Enhance the Performance of High-Gain Silicon-Graphene Photodetectors – F. De Geronimo, N. Renno

3.1 Abstract

Graphene-silicon photodetectors have high gain, but this gain varies under changing environmental conditions. We developed a stabilization circuit that mitigates this problem by maintaining the graphene channel current nearly constant by self-adjustments of the voltage across the graphene. We show that prototype devices with this circuit have a 2–4x smaller dark current noise power across temperatures ranging from −5°C to 55°C, and ~4x lower noise power under modulated laser forcing with parasitic background white light. These results show that the device responsivity remains high under the changing environmental conditions. They demonstrate that the proposed stabilization circuit significantly improves performance of graphene-silicon photodetectors, enabling practical applications such as in optical tracking, alignment, and low-flux sensing.

This chapter describes a published journal article: F. G. De Geronimo and N. O. Renno, "Low-Noise Stabilization Mechanism to Enhance the Performance of High-Gain Silicon-Graphene Photodetectors," in IEEE Sensors Letters, vol. 9, no. 12, pp. 1-4, Dec. 2025, Art no. 7005704, doi: 10.1109/LSENS.2025.3633998.

3.2 Motivation & Proposed Stabilization Mechanism

3.2.1 Motivation

Photodetectors based on graphene-silicon heterostructures have the potential to overcome some of the limitations of conventional photodetectors because they combine the high absorption of semiconductor materials with the rapid carrier mobility capacity of graphene [1-4]. Responsivities approaching ~10^7 A/W have been reported in the literature, making graphene-silicon devices promising for low-flux applications [4, 5], but they suffer from highly nonlinear photoresponse and high sensitivity to variations in environmental conditions [5, 6]. We address these challenges with a novel electronic stabilization circuit that actively regulates the graphene channel current, enhancing signal stability across varying illumination and ambient temperature.

3.2.2 Proposed Stabilization Mechanism

The stabilization mechanism circuit we developed is illustrated in Figure 24. The drain is connected to an operational amplifier with a negative feedback resistor (R_F) and capacitor (C_F) to produce a transimpedance amplifier which converts the graphene current into a voltage. The feedback also guarantees that the voltage at the drain electrode (V_D) equals the bias voltage V_{DD} applied to the positive input of the amplifier. The source is connected to a current source (I_S) in parallel with a capacitor (C_S), both of which are connected to ground.

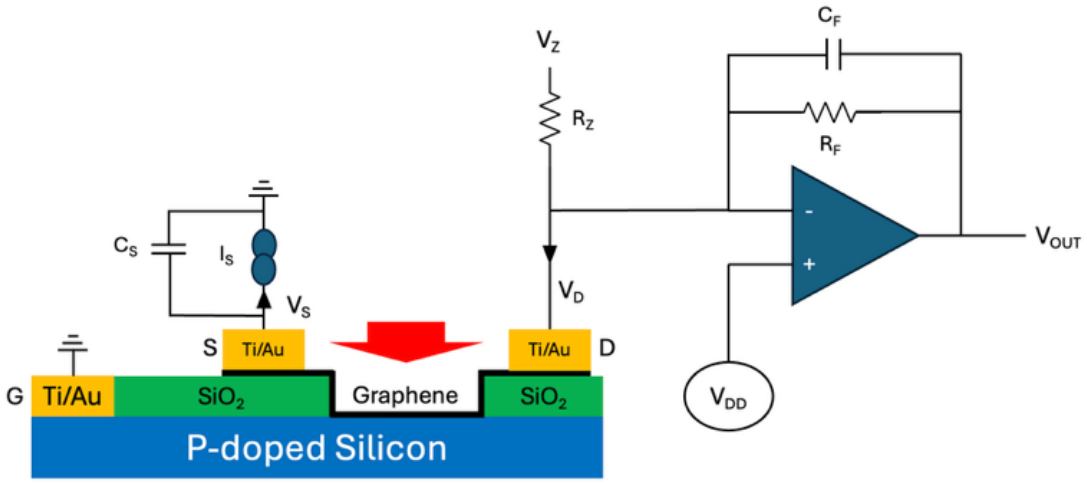


Figure 24. The detector design and associated stabilization mechanism electronics. The source is connected to the source capacitor (C_S) and the current source (I_S), which help regulate the source voltage (V_S). The drain is connected to the zeroing resistor (R_Z), the zeroing voltage (R_V), the feedback capacitor (C_F) and resistor (R_F), the user-set drain voltage (V_{DD}), the true drain voltage (V_D), and the output voltage of the system (V_{OUT}).

The mechanism works by setting the operating current in the graphene to a specific value, as determined by I_S (e.g., 600 µA), while the source voltage V_S self-adjusts to meet this current requirement when the resistance of the graphene changes. The value of C_S is adjusted, in combination with the graphene resistance, to provide a high-pass filter tuned to accommodate the frequency range of the signals of interest. When a modulated signal is incident on the device, the source node exhibits a low impedance thus allowing the signal to flow through the transimpedance amplifier at full gain. On the other hand, when low-frequency fluctuations occur, either from temperature or from other environmental factors such as light, the source adjusts to reject the amplification of those undesired noise components.

While a solution for filtering low frequency noise could be implemented with a high pass filter at the output of the transimpedance amplifier, the proposed stability mechanism is an improvement to this approach because it stabilizes the charge carrier density in graphene and ensures the device operates within the limits of the front-end electronics. Graphene's electrical conductivity is highly sensitive to changes in charge carrier density, which can be significantly

influenced by environmental factors such as temperature and relative humidity [11]. A constant charge carrier density within the graphene mitigates these environmental effects and leads to a higher resolution. Moreover, for large environmental changes, the proposed stability mechanism prevents the possibility of front-end electronics saturation by fixing the operating current. This allows for use in environments with extreme fluctuations.

The source voltage V_S, which responds to environmental changes and low-frequency fluctuations, can be used to monitor the operating point of the graphene, to provide calibration data and, if desired, to provide an additional feedback mechanism through the gate voltage, thus further improving the stability of the response.

The current source I_S has been designed to contribute with negligible noise. The optional voltage V_Z and resistor Rz allow zeroing the amplifier DC output.

3.3 Testing Setup & Device Characterization

The Silicon-graphene detector with and without the stabilization mechanism was characterized at different temperatures in both dark and background (parasitic) light conditions. Three tests were conducted to fully characterize the effectiveness of the stabilization mechanism.

3.3.1 Room Temperature Optical Characterization Test Setup

A schematic of the optical characterization setup is shown in Figure 25. A 2.5 mW, 635 nm laser diode was focused onto the device-under-test (DUT) using a three-lens aspheric optical system. The minimum optical spot size was measured using a standard CMOS camera and verified to be smaller than the detector active area. This verification was critical for accurate responsivity calculations, as it ensured that the total incident optical power was fully contained within the active region of the device.

The laser diode was driven using a commercially available laser driver circuit connected to a power supply and the waveform generator of the Analog Discovery 3 platform. The waveform generator provided the modulation signal required to operate the stabilization mechanism at the desired frequencies.

To achieve accurate alignment of the laser spot on the detector surface, the DUT was mounted on a three-axis linear translation stage. The detector position was adjusted until the measured photoresponse was maximized, ensuring that the focused laser spot was entirely incident on the active area. Although this alignment procedure was time-intensive, the stage position was fixed after optimization to maintain consistency across subsequent measurements.

The drain and source voltages were controlled through the stabilization circuit interfaced with the Analog Discovery 3, while the gate electrode remained grounded because the drain-source bias provided the required electric field across the junction. The output voltage from the transimpedance amplifier was monitored using the oscilloscope function of the Analog Discovery 3. The resulting photocurrent was then determined by dividing the measured output voltage by the feedback resistance of the amplifier circuit.

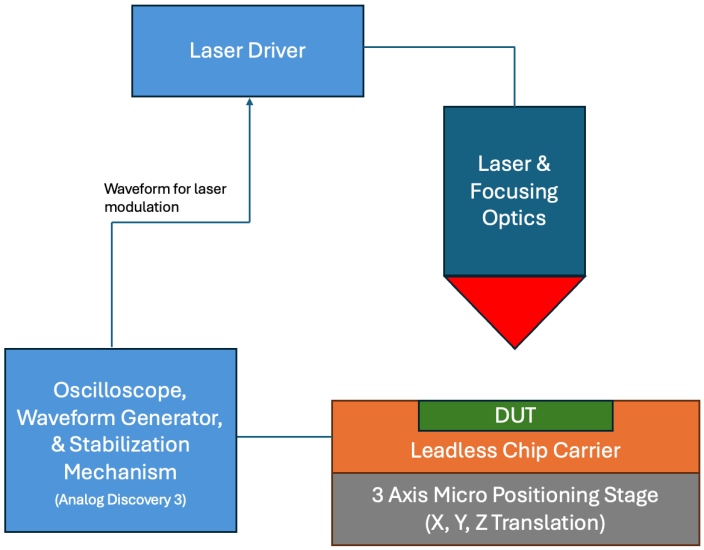


Figure 25. Schematic of the optical characterization setup used to evaluate the silicon-graphene photodetectors. A 635 nm laser diode, driven by a commercially available laser driver and modulated using the Analog Discovery 3 waveform generator, was focused onto the device-under-test (DUT) through a three-lens aspheric optical system. The DUT was mounted on a three-axis translation stage for precise alignment of the laser spot onto the detector active area. The stabilization circuit controlled the drain-source bias, while the output photoresponse was measured using the oscilloscope functionality of the Analog Discovery 3.

3.3.2 Variable Temperature Optical Characterization Test Setup

For variable temperature optical characterization of the detectors with/without the stabilization mechanism, the test setup above was moved into a large temperature chamber. However, data extraction from the oscilloscopes required a live connection to a computer, and thus, BNC cable adapters were used to connect the interior test setup to a computer outside. Additionally, to prevent excessive moisture and condensation when transitioning from sub-zero temperatures to warmer temperatures, desiccant beads were spread out within the chamber. An image of our test setup inside the temperature chamber is shown in Figure 26.

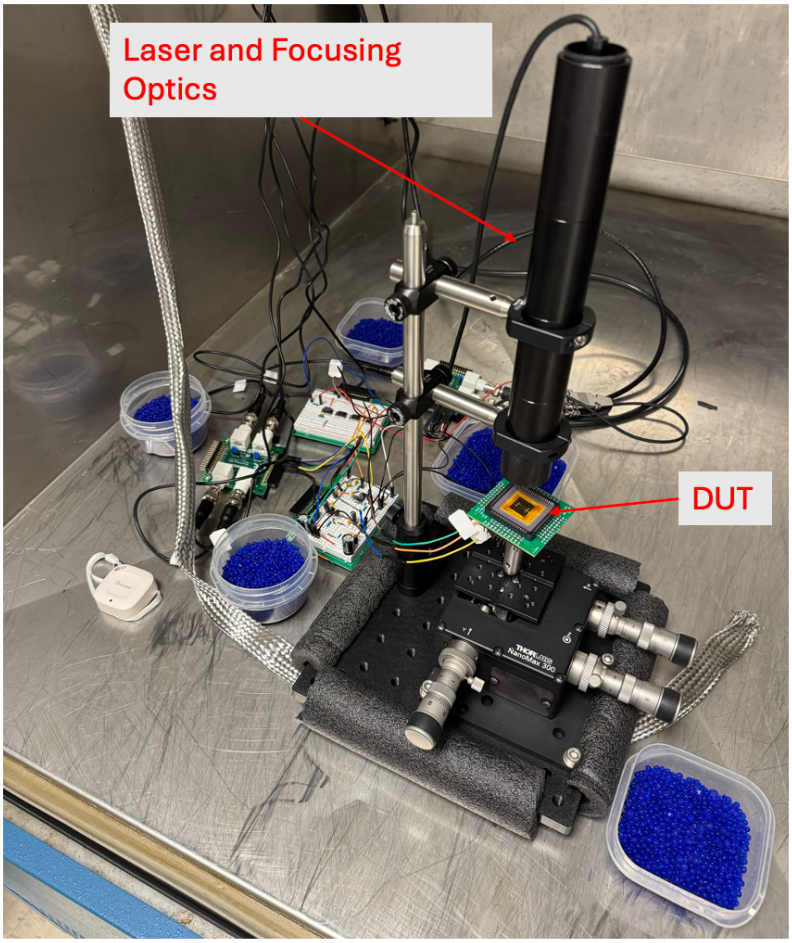


Figure 26. Optical testing setup used for device characterization in the temperature chamber. Blue desiccant beads placed in plastic bowls are used to control humidity within the enclosure, while a Bluetooth temperature sensor (white component to the left of the setup) monitors the local thermal environment during measurements. Foam padding beneath the optical breadboard helps dampen vibrations, particularly during temperature chamber cooldown, ensuring stable and low-noise data acquisition. A thick metal ribbon was also used to provide a robust common ground between the inside and outside of the chamber.

Since laser diodes are sensitive to the environmental temperature, the laser was calibrated at different temperatures to ensure that the incident power was kept constant across the entire swept temperature range. This was done by fixing the power meter outside the transparent window of the temperature chamber while the laser was subject to various temperatures inside the chamber. Power losses across the transparent window were measured and found to be minimal.

3.3.3 Characterization Tests

The silicon-graphene detector with and without the stabilization mechanism was characterized at different temperatures in both dark and background (parasitic) light conditions. For experiments without stabilization, the source becomes voltage controlled as in traditional transimpedance configurations [7,8]. The oscilloscope settings were fixed at 8M samples at a rate of 1MHz to allow for comprehensive long-term data capture.

To evaluate the stabilization mechanism, three tests were conducted. First, dark current measurements were taken at various environmental temperatures. The detector and stabilization electronics were placed in a temperature-controlled chamber under near-total darkness, where temperatures were varied from -5°C to +55°C in 10°C increments with 5-minute dwell times. Dark current and noise, expressed as the full width at half maximum (FWHM) of the spectral line, were recorded using an oscilloscope. Second, the detector's photoresponse was measured under constant laser illumination. A 635 nm laser diode, calibrated for ~1 μW output at 5°C and 33°C, was used to illuminate the detector inside the temperature chamber, and measurements were taken at both temperatures with 5-minute dwell times. The temperature range was limited to 33°C due to the laser's operational constraints. Finally, the system's robustness to parasitic light was tested at room temperature (25°C). A 635 nm laser modulated at 3 kHz was used to compare detector responses with and without stabilization, both in darkness and under a 120 Hz overhead white light. The detector response was then recorded with only the white light to assess suppression of the parasitic illumination.

3.4 Results

3.4.1 Device Dark Current Measurements at Various Temperatures

Figure 27A shows the FWHM of the device current versus changing temperature for the detector with and without the stabilization mechanism. Without the mechanism, the FWHM stays flat at approximately 0.5 μA until around 15°C and then increases rapidly as temperature increases, reaching nearly 1.3 μA. In comparison, the stabilization mechanism effectively lowers the FWHM at all tested temperatures, achieving nearly half the FWHM at 55°C of the system without stabilization. Indeed, the FWHM at 35°C with stabilization, averaging 0.52 μA, is comparable to the FWHM at -5°C without the stabilization mechanism, increasing the effective operating temperature range of these devices.

Moreover, along with reducing the noise, the stabilization mechanism effectively decreases the device's dark current dependence on the temperature as shown in Figure 27B. Large swings and variations in the dark current are seen in the device without the stabilization mechanism but strongly mitigated in the device with the stabilization mechanism. For instance, at 35°C, for the system without stabilization we captured dark current magnitudes between approximately 1.2 mA and 1.26 mA (about 5%), while with stabilization, we captured dark current magnitudes between 1.26 mA and 1.27 mA (about 0.8%), a far slimmer range.

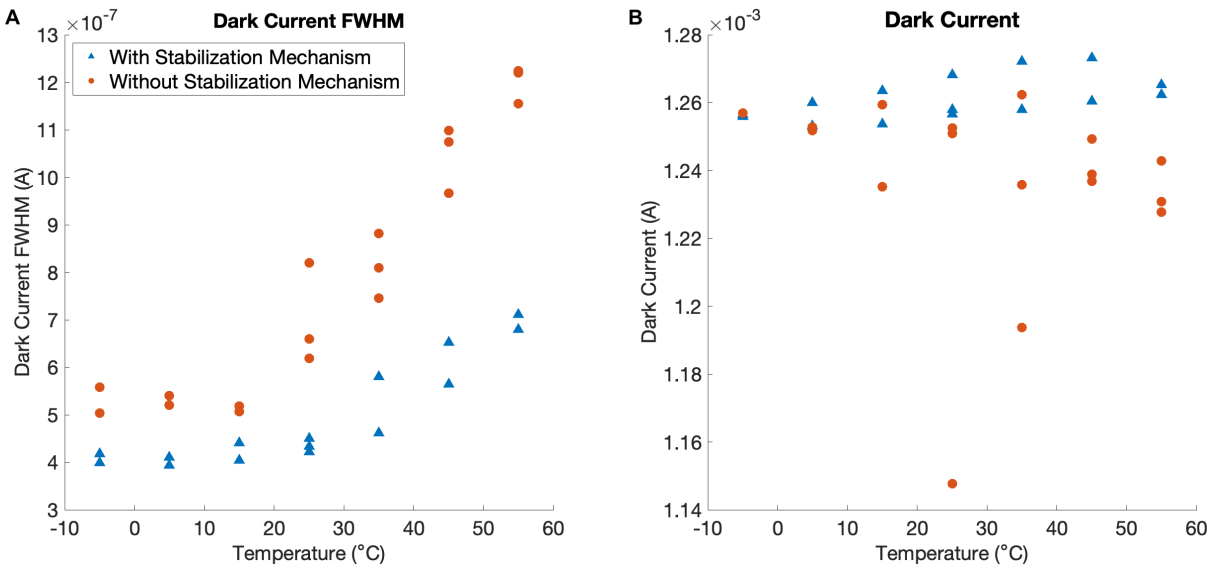


Figure 27. (**A**) Dark Current FWHM with and without the stabilization mechanism at various temperatures. The stabilization mechanism effectively reduces noise across the entire tested temperature range. (**B**) Dark Current with and without the stabilization mechanism at various temperatures. The variability in dark current without the stabilization mechanism is visibly greater than that with stabilization.

3.4.2 Device Photoresponse with Constant Incident Laser Power at High and Low Temperatures

In warm and cold environments, the feedback mechanism effectively suppresses the low-frequency noise under constant illumination. When illuminated at constant power, noise is expected from the statistics in the generation of the electron-hole pairs. Additional non-negligible fluctuations may occur from the light source fluctuations and from the entire conversion gain process (from light input to current output), due to environmental factors. The proposed mechanism stabilizes the response as well. At 5°C, the FWHM with the feedback mechanism was on average 1.5 mV, nearly half of the FWHM without the stabilization mechanism, 2.9 mV. At 33°C, the stabilization mechanism maintained a very low FWHM of 1.7 mV, while the system without the stabilization circuit suffered from much higher noise, with an average FWHM of 4.2 mV. This difference in FWHM corresponds to a factor six reduction in noise power. The stabilization mechanism effectively reduces low frequency noise at both low and high

temperatures, achieving significantly lower noise at 33°C than the detector without the stabilization mechanism at 5°C. This provides an optimistic outlook for the use of the proposed mechanism for improved detector performance at higher operating temperatures and over a broader range of temperatures.

3.4.3 Room Temperature Laser Modulation with and without "Noisy" White Light

Despite a "noisy" 120 Hz white light overhead, the stabilization mechanism effectively suppressed this low-frequency component while maintaining high gain sensitivity to the rapidly modulated laser light. Figure 28 shows the response spectra for the three experiments, (A) no laser with parasitic white light on, (B) modulated laser with parasitic white light off, and (C) modulated laser with parasitic white light on.

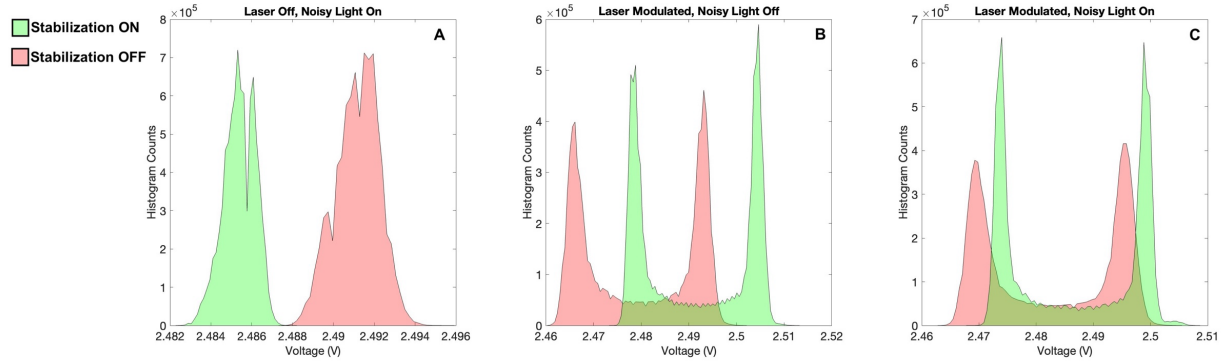


Figure 28. Response spectrum of the detector when (**A**) illuminated by only the low frequency white light, (**B**) illuminated by the high frequency modulated laser, and (**C**) illuminated by both the low frequency white light and the high frequency modulated laser.

When the laser is kept off and the detector is subject to incident light from the 120 Hz white light source, the stabilization mechanism reduces the FWHM of the response spectrum from 2.2 mV to 1.8 mV. This is directly observed in Figure 28A with the thinning of the spectral line when the stabilization is active (green).

When the laser is modulated fast enough (>3kHz) for the signal to bypass the low frequency filtering of the stabilization circuit, we clearly observe the two spectral lines from the modulating

square wave. There is no loss in gain or signal response compared to the system without stabilization since the distance between the two peaks is equivalent in both cases. However, the thinning and vertical elongation of the peaks indicates a visible reduction in the FWHM. In Experiment B (laser on, white light off), the average FWHM of the two peaks with the stabilization mechanism active was 3.0 mV, compared to 4.2 mV when the stabilization mechanism was not active, corresponding to a factor two in noise power. Low frequency noise components from fluctuations in the laser, environmental light, changes in temperature, and overall noise of the system are effectively reduced in the system with stabilization.

These improvements become clearer in Experiment C when the parasitic white light is turned on with the modulated laser. The white light introduces additional low frequency noise which is filtered out by the stabilization mechanism. The peaks of the response spectrum are greatly sharpened with the stabilization mechanism, indicating lower noise operation. Indeed, the average FWHM of the two peaks with the stabilization mechanism active was 2.4 mV, compared to 4.7 mV when the stabilization mechanism was not active, corresponding to an approximate factor four in noise power. This reduction in noise comes at no cost of the gain of the system, since the separation of the peaks is identical with and without the stabilization mechanism. Thus, we can cleanly capture a modulated signal while maintaining a stable operating point and filtering out unwanted low frequency noise, all while taking advantage of the high-gain graphene-Silicon mechanism.

3.5 Conclusion & Future Work

The stabilization circuit we propose significantly improves the performance of graphene-silicon photodetectors under variable conditions. Indeed, devices with this circuit have up to 4x reduction in dark current noise power across temperatures from −5°C to 55°C, and ~4x lower noise

power under modulated laser with parasitic white light, all while experiencing no loss in signal strength. In the next chapter, we integrate this circuit into a quad-cell detector configuration to enable precise alignment using low-power modulated laser signals, extending its applicability to active tracking and optical sensing systems.

3.6 References

[1] Wang, X., Cheng, Z., Xu, K. *et al.* High-responsivity graphene/silicon-heterostructure waveguide photodetectors. *Nature Photon* **7**, 888–891 (2013). https://doi.org/10.1038/nphoton.2013.241

[2] Yu, J., Zhong, J., Kuang, X. *et al.* Dynamic Control of High-Range Photoresponsivity in a Graphene Nanoribbon Photodetector. *Nanoscale Res Lett* **15**, 124 (2020). https://doi.org/10.1186/s11671-020-03352-7

[3] A. K. Geim, Graphene: Status and Prospects.*Science***324**,1530-1534(2009). DOI:10.1126/science.1158877

[4] Liu F, Kar S. Quantum Carrier Reinvestment-induced ultrahigh and broadband photocurrent responses in graphene-silicon junctions. ACS Nano. 2014 Oct 28;8(10):10270-9. doi: 10.1021/nn503484s. Epub 2014 Oct 17. PMID: 25325405.

[5] Liu, J., Yin, Y., Yu, L. *et al.* Silicon-graphene conductive photodetector with ultra-high responsivity. *Sci Rep* **7**, 40904 (2017). https://doi.org/10.1038/srep40904

[6] Su, Fang, et al. "Long-Term Stability of Photodetectors Based on Graphene Field-Effect Transistors Encapsulated with Si3N4 Layers." *Applied Surface Science*, vol. 459, Nov. 2018, pp. 164–170, https://doi.org/10.1016/j.apsusc.2018.07.208. Accessed 20 Apr. 2025.

[7] Iqbal, S., Imran, H., Qasim, U. B., & Butt, N. Z. (2017). Design of high performance graphene/Silicon photodetectors. *2017 International Conference on Simulation of Semiconductor Processes and Devices (SISPAD)*, 205–208. https://doi.org/10.23919/sispad.2017.8085300

[8] Butt, Nauman Z., et al. "Substrate-Induced Photofield Effect in Graphene Phototransistors." *IEEE Transactions on Electron Devices*, vol. 62, no. 11, Nov. 2015, pp. 3734–41. *DOI.org (Crossref)*, https://doi.org/10.1109/TED.2015.2475643.

[9] Meca Meca, F.J.; Martín-Gorostiza, E.; García-Garrido, M.Á.; Salido-Monzú, D. Phase Stability under Thermal Drifts in Photodiode-Conditioning Transimpedance Amplifiers for Distance Metrology. *Sensors***2021**, *21*, 3455. https://doi.org/10.3390/s21103455

[10] Ferrari, A., Basko, D. Raman spectroscopy as a versatile tool for studying the properties of graphene, *Nature Nanotech* **8**, 235–246 (2013). https://doi.org/10.1038/nnano.2013.46

[11] Quellmalz, A., Smith, A. D., Elgammal, K., Fan, X., Delin, A., Östling, M., Lemme, M., Gylfason, K. B., & Niklaus, F. (2018). Influence of Humidity on Contact Resistance in Graphene Devices. *ACS applied materials & interfaces*, *10*(48), 41738–41746. https://doi.org/10.1021/acsami.8b10033

Chapter 4 Silicon-Graphene Quadrant Detector for Precision Low-Flux Laser Alignment

4.1 Abstract

Silicon-based quadrant detectors are utilized in many applications, including autocollimators, optical trackers, atomic force microscopes, and stage positioners. However, native silicon photodiodes have low responsivity ($R < 0.7$ A/W), limiting their effectiveness in low-flux applications. We present a novel quadrant detector architecture that utilizes a graphene-silicon junction to significantly enhance device responsivity while maintaining low operating voltage and competitive noise performance. L-shaped graphene strips are introduced in our design to achieve uniform response in four-quadrant quantum gain-enhanced detectors. Measured individual quadrant responsivities were between ~10 and ~23 A/W, up to about 30× greater than silicon's native responsivity. Device dark current noise was measured, and NEP is estimated to be comparable to commercially available solutions, while pixel crosstalk is ~5%. Finally, a 40 μm laser spot was precisely tracked over the 60 μm × 60 μm active area, demonstrating high response and linear functionality once calibrated.

This chapter describes an article submitted to IEEE Sensors Letters as: F. G. De Geronimo and N. O. Renno, "Silicon-Graphene Quadrant Detector for Precision Low-Flux Laser Alignment."

4.2 Introduction

Silicon quadrant detectors (quad-cells) are widely used in precision optical metrology and positioning systems, including autocollimators, optical trackers, scanning probe microscopes, beam centering systems, sun sensors, and ultra-precision displacement and alignment instruments [1]. Despite their broad adoption, conventional silicon quad-cells exhibit responsivities of ~0.7 A/W [2], which limits sensitivity in low-flux optical tracking applications. Furthermore, these devices typically require operating voltages between 5 V and 15 V, and frequently higher [3], restricting their integration into low-power systems and limiting sensitivity in applications requiring detection of weak optical signals.

Graphene-silicon heterojunction photodetectors provide a promising path to overcome these limitations by enabling extremely high responsivity at low operating voltages. While prior graphene-silicon detectors exploiting this high-gain mechanism have demonstrated substantial sensitivity improvements, they have largely been confined to single-pixel implementations because their electrode geometries require contacts on opposite sides of the active region [4,5]. Here, we introduce a novel quadrant detector architecture based on L-shaped graphene channels that optimizes electrode placement and enables a true quad-cell configuration while preserving the high-gain, low-voltage operation of graphene-silicon heterojunction devices.

4.3 Quadrant Detector Device Architecture

4.3.1 Quadrant Detector Device Design

Our device is based on a novel architecture that enables pixels to be adjacent to each other while still maintaining the high quantum gain from the graphene-silicon junction. A microscope image of our device is shown in Figure 29.

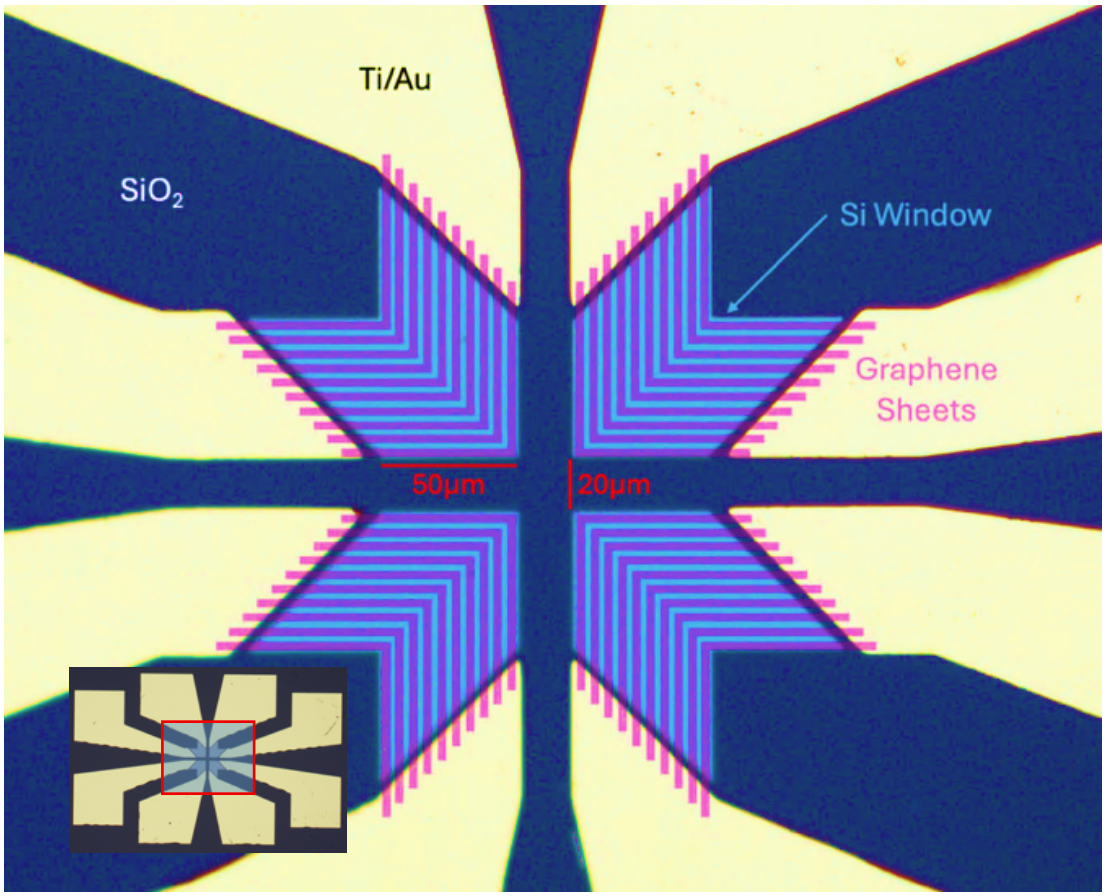


Figure 29. Microscope image of our novel quadrant detector device. The dark background region is the SiO2, the yellow regions are the Ti/Au electrodes, the light blue arrow regions are the silicon windows, and the purple strips are the areas where the graphene was patterned into parallel strips. Each graphene strip is 3 μm wide, and the strip separation is 2 μm. The total effective length of each strip is approximately 100 μm.

L-shaped graphene strips were employed instead of conventional straight channels to enable the four pixels to be arranged in a true quadrant configuration while maintaining a minimum inter-pixel spacing of 20 μm. This geometry allows the active regions to converge toward the center of the device without introducing abrupt channel length variations. To the best of our knowledge, L-shaped graphene strips have not previously been reported for quadrant photodetector applications, and their use here enables both compact pixel spacing and uniform electrical characteristics across the detector.

In addition, to improve current uniformity across the underlying silicon window, the graphene was patterned into multiple parallel strips rather than a single continuous channel. This

strip-based architecture constrains carrier transport to well-defined, repeatable pathways, reducing sensitivity to local inhomogeneities in graphene quality and contact resistance. Moreover, it enables more straightforward quantification of the effective graphene channel resistance, as carriers are forced through nominally identical conduction routes. Each graphene strip was designed to be 3 μm wide and 2 μm away from adjacent strips, with each strip having a total effective channel length of approximately 100 μm.

According to the quantum gain model proposed by Liu and Kar [4], the photoconductive gain—and thus the responsivity—scales inversely with the square of the graphene channel length. As a result, spatial variations in channel length would lead to non-uniform responsivity across the detector. The arrow geometry was therefore selected to maintain identical graphene strip lengths throughout the active region, thereby promoting uniform gain enhancement across the silicon window.

For the same reason, the source and drain electrodes were designed to interface with the graphene strips at an angle rather than orthogonally. This angled electrode configuration ensures that each graphene strip has an equal effective channel length between contacts, minimizing strip-to-strip variations in resistance and photoconductive gain. Together, these design choices enable spatially uniform responsivity while preserving the geometric symmetry required for accurate quadrant-based position sensing.

4.3.2 Circuit Design & Test Setup

Our quadrant detector employs the electronic stabilization and readout architecture introduced in our previous work [6]. The drain electrode of each pixel is connected to a transimpedance amplifier (TIA) consisting of an operational amplifier with a 2 kΩ feedback resistor and 47 pF feedback capacitor, converting the graphene drain current into a voltage signal

while fixing the drain voltage at a user-defined bias. This configuration provides stable graphene channel biasing and a well-defined current-to-voltage conversion for position-sensitive measurements.

Stabilization is achieved by enforcing a fixed operating current in the graphene channel (250 μA) using a current source connected to the source electrode, with a parallel 47 nF capacitor that allows the source voltage to self-adjust to slow changes in graphene resistance. This suppresses low-frequency fluctuations caused by environmental effects or optical drift while allowing modulated optical signals to reach the TIA at full gain. The graphene resistance and source capacitance define a high-pass response, while the readout electronics set the upper bandwidth limit, resulting in an effective bandpass over the measurement frequency range.

Unlike conventional output-stage high-pass filtering, this approach directly regulates graphene carrier density, reducing environmental sensitivity, preventing front-end saturation under large background signals, and maintaining stable matched gain across quadrants while allowing the source voltage to be monitored as a diagnostic [6].

For optical characterization, the device was illuminated with a 635 nm pigtail laser capable of being focused to ~10 μm, verified with a calibrated camera. The laser was modulated at 2.5 kHz to activate the stabilization mechanism. The detector was mounted beneath the laser on a precision three-axis stage with micrometer-scale resolution, enabling controlled raster scans across the active area to map quadrant responsivity, active regions, and pixel cross-talk.

4.4 Device Characterization Setup

Compared to the optical characterization setup for a single detector, the characterization of the quadrant detector required more precise knowledge about the profile of the incident laser.

4.4.1 Testing Setup & Laser Profile Verification

The experimental setup used to characterize the fabricated silicon-graphene quadrant detectors is shown in Figure 30. The setup was designed to enable precise optical alignment, controlled beam positioning, and accurate measurement of the detector response as the incident laser spot traversed the detector surface. Many components of the setup were carried over directly from the characterization system described in Chapter 3, including the low-noise electronic readout circuitry, translational stage, and chip carrier socket used to mount and electrically interface with the detectors. Reusing this infrastructure enabled consistency between detector studies while reducing variability introduced by changes in the measurement system.

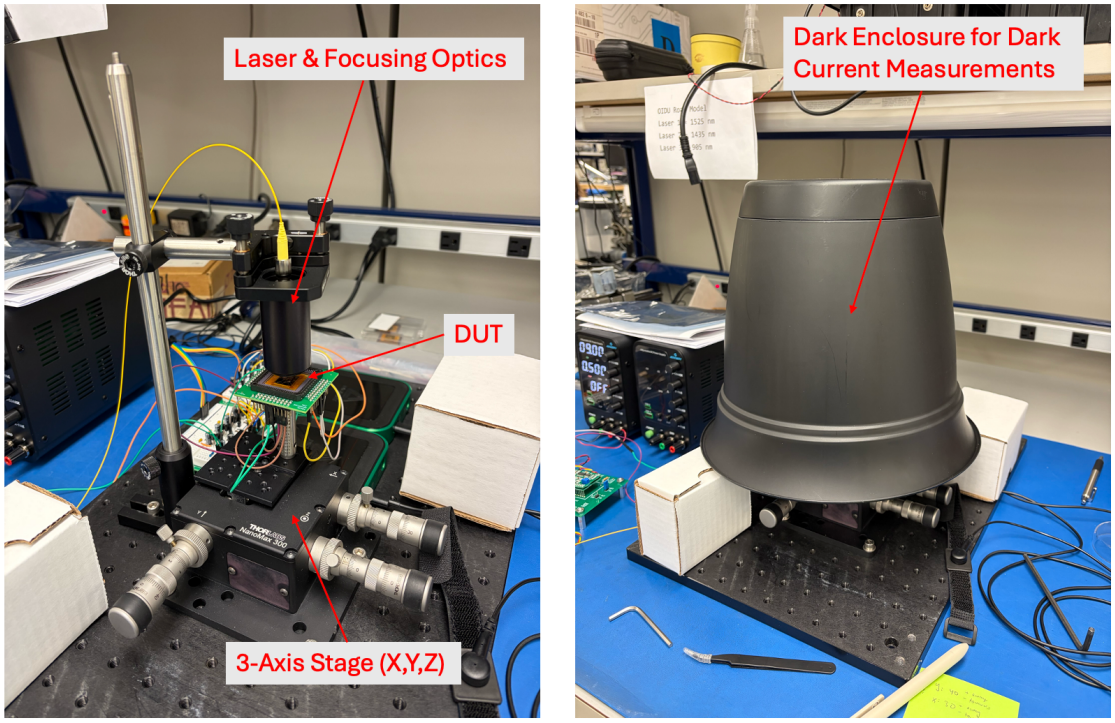


Figure 30. Experimental optical characterization setup used for quadrant detector testing. (**Left**) Optical setup consisting of a lens tube assembly used to focus the laser to an approximately 20 µm spot size, the device under test (DUT) mounted on a three-axis translation stage for precise positioning, and electrical connections routed from the DUT to custom circuits housed on breadboards compatible with the Analog Discovery 3. (**Right**) The same setup shown with the light-blocking enclosure used to ensure dark measurement conditions during dark current characterization with overhead lighting turned off.

Compared to the setup presented in Chapter 3, the optical lens stack used in this work was simplified and reduced in size. This modification decreased the overall complexity of the optical path while still enabling sufficient beam focusing performance for quadrant detector measurements. The reduced lens stack also improved alignment efficiency and minimized the number of optical elements contributing to aberrations or alignment sensitivity. An additional tip-tilt mount for the lens tube was introduced to minimize angular misalignment between the laser and the DUT.

Moreover, a black enclosure was placed over the DUT (Figure 30, right) to enable reliable dark current measurements. Although the overhead lights were turned off during testing, residual light emitted from nearby instruments, such as the computer monitor and power supply displays, could still influence the measurements. The enclosure therefore provided complete optical isolation of the detector, ensuring characterization under true dark conditions.

A critical aspect of quadrant detector characterization is accurate knowledge of the incident laser beam profile and spot size. Since quadrant detectors operate by comparing photocurrent generated across spatially separated detector regions, the measured response depends strongly on the spatial intensity distribution of the incoming beam. As a result, characterization of the laser profile was necessary to properly interpret detector response as the beam was translated across the device surface.

The measured laser spot profile is shown in Figure 31. This beam profile was extracted using a simple CMOS profiling camera. The beam is observed to be well focused near the center of the profile, with slight asymmetries appearing away from the beam center. These asymmetries are attributed to minor optical aberrations and alignment imperfections within the imaging system. Despite these effects, the beam maintained a sufficiently localized and stable profile for detector

characterization. Knowledge of the beam profile was essential for understanding the quadrant detector response, particularly during beam scanning experiments in which the laser position was incrementally translated across the detector active area.

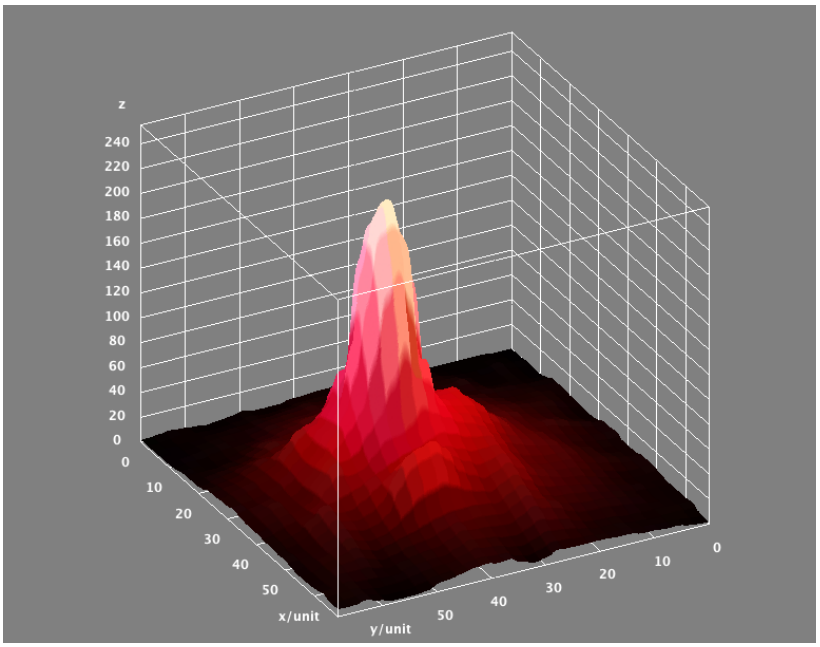


Figure 31. Three-dimensional intensity profile of the focused laser spot measured using a CMOS camera. The spatial dimensions are shown in microns, with the minimum spot diameter measured to be approximately 20 μm at focus. The beam exhibits slight asymmetry, likely arising from minor optical aberrations and alignment imperfections within the imaging system.

4.5 Results

This section evaluates the key performance characteristics of the fabricated silicon-graphene quadrant detector, including dark current noise, responsivity, active area distribution, and position sensitivity. Together, these measurements provide insight into the detector's sensitivity, uniformity, and suitability for precision optical sensing applications.

4.5.1 Device Dark Current & Noise

Each quadrant's dark current noise was evaluated at room temperature while the device was maintained in near-total darkness to isolate intrinsic noise from optical contributions. Because the noise currents could be masked by the noise of the oscilloscope, a multi-stage high-gain, low-

noise amplification was added to the system. This approach ensured that the measured spectra were dominated by device noise rather than oscilloscope input noise. The resulting dark current noise spectral densities for all four quadrants are shown in Figure 32.

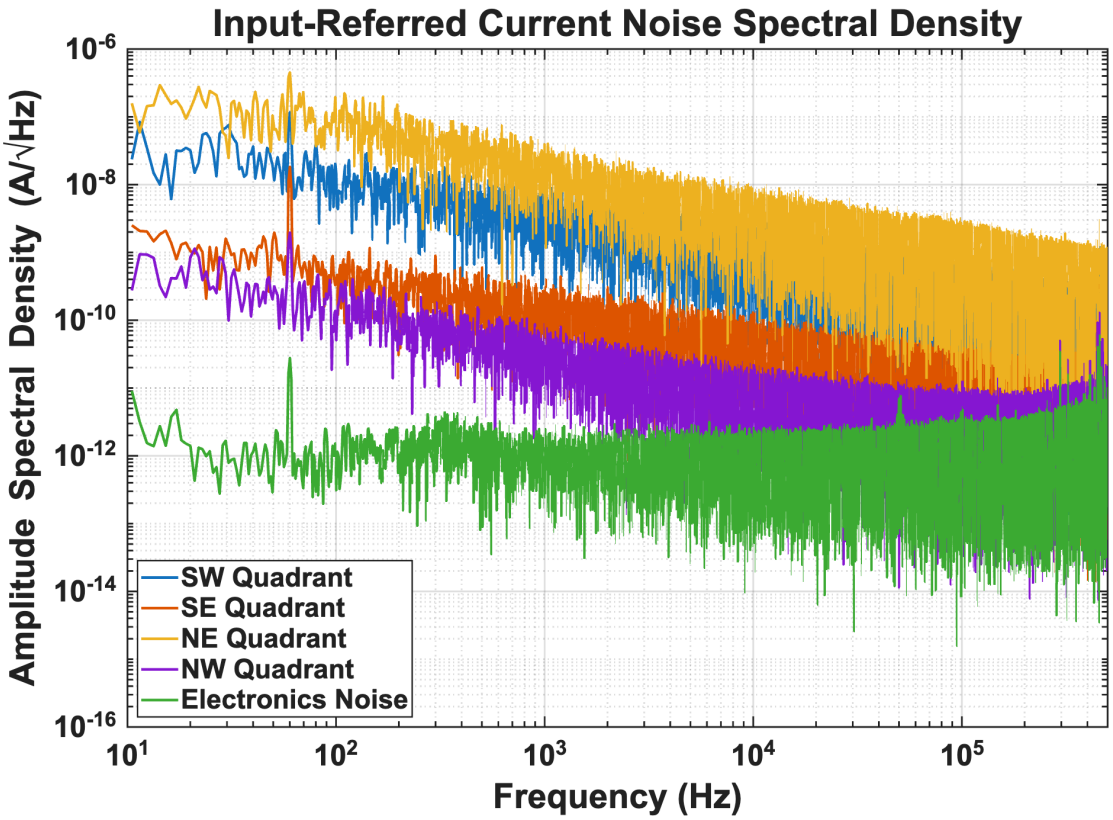


Figure 32. The dark current noise spectrum is plotted for the four quadrants. The noise from the electronics (i.e. replacing the device with a resistor of value equal to the graphene resistance) is also plotted to verify that the visible noise contributions are indeed from the quadrant detector. Peaks near 60 Hz are likely due to induced noise from the utility power during testing.

Among all quadrants, the northeast (NE) pixel exhibited the highest measured dark current noise, while the northwest (NW) pixel showed the lowest. The dark current varied significantly across quadrants, likely due to differences in graphene strip quality, variations in strain across the graphene regions, and the presence of possible defects. Notably, this variation in dark noise does not correlate with the measured responsivity across the device: the NW quadrant, despite having the lowest noise, demonstrated the lowest responsivity, whereas higher-noise quadrants such as the NE and SW maintained substantially larger responsivities. This lack of correlation indicates

that the dominant factors governing photoconductive gain and responsivity in the graphene-silicon heterojunction are largely independent of the mechanisms contributing to dark current noise. Moreover, although the quadrants exhibit higher dark current noise than conventional silicon quadrant detectors, the enhanced responsivity of the graphene-silicon architecture maintains a noise-equivalent power (NEP) for the SE and NW pixels comparable to that of commercially available devices [2,9]. Indeed, at the noise frequency point of 10 kHz, the SE and NW quadrants exhibit NEP values of 0.66 $pW/\sqrt{Hz}$ and 0.9 $pW/\sqrt{Hz}$, respectively. The resulting signal-to-noise ratio (SNR) ranged from 14.7 to 3,586 depending on the quadrant, primarily determined by the measured dark current.

These results highlight the robustness of the detector architecture. The device maintains strong responsivity and usable sensitivity across all pixels without requiring stringent matching of dark current characteristics, supporting the viability of this approach for multi-pixel and quadrant detector implementations.

4.5.2 Device Active Area & Responsivity

A raster scan of the device was completed using a 20 μm spot size and steps of 10 μm in X and Y. The device active areas were identified, as shown in Figure 33 (left).

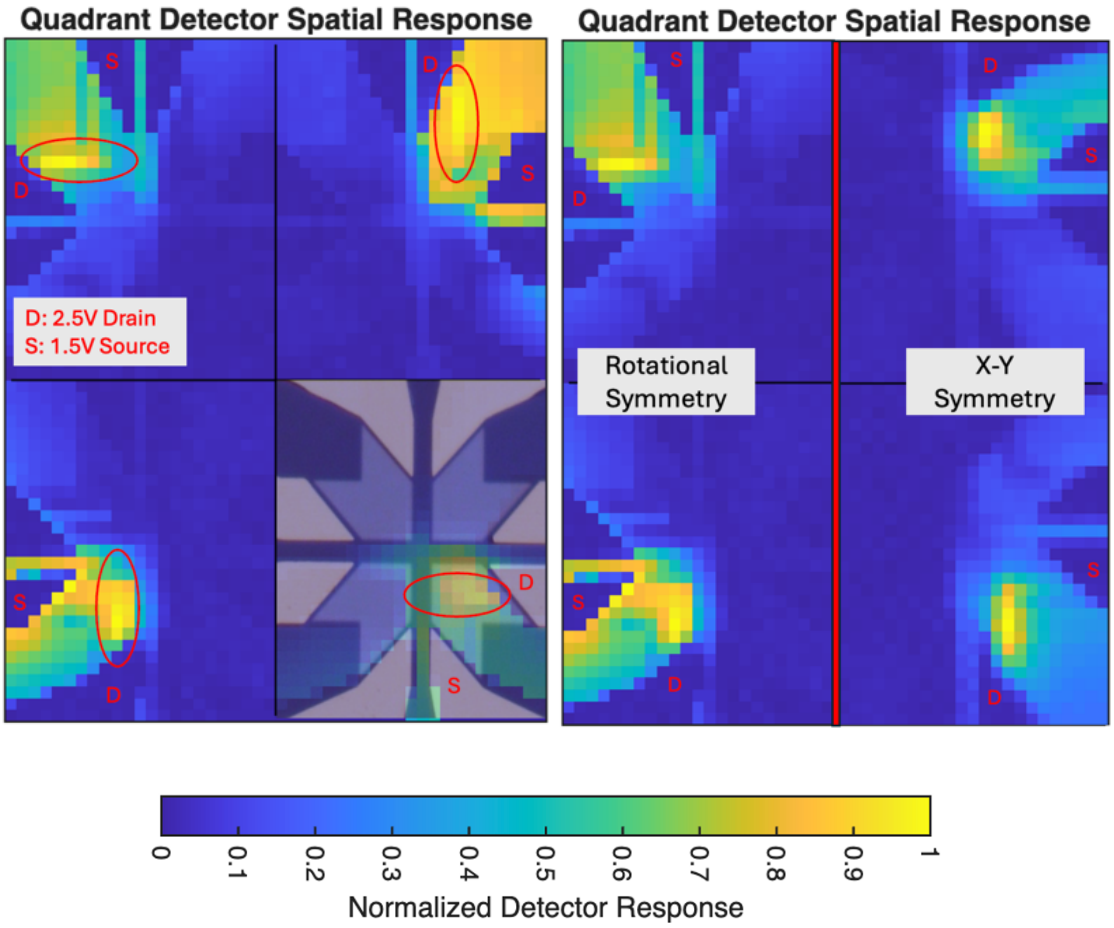


Figure 33. (**Left**) Detector response extracted from a raster scan of entire detector area using a 20 µm wide 635 nm 2 µW laser. The source (S) and drain (D) are labeled for each quadrant, and the lower right quadrant has an image of our detector overlayed to show that features like the gold electrodes and SiO_2 areas are captured in the scan. (**Right**) Comparison of device active areas for rotational and X-Y symmetry device configurations. For rotational symmetry, the drain and source alternate as you go around the device (D, S, D, S, etc.), while for X-Y symmetry, the sequence of drain and source is D, D, S, S, etc.

Measurements indicate that the sensitivity of our device is highest on the side of the graphene channel closest to the drain electrode, likely due to the higher gate bias in this region arising from the drain's elevated voltage relative to the source. Based on this result, the optimal device configuration features alternating drain/source connections around the device, providing rotational symmetry and uniform sensitivity in all directions. Raster scans of the device active area performed under configurations in which the drain and source electrodes are mirrored along the X and Y axes indicate that the effective active region becomes slightly constrained along one

measurement axis (Figure 33, right). Moreover, pixel cross-talk between adjacent quadrants was measured to be approximately 5%, indicating minimal interference and good quadrant isolation.

Maximum responsivity was recorded for each quadrant using our 2 μW modulated laser focused on the detector, with the highest measured value of 22.7 A/W for the southeast (SE) quadrant and the lowest of 10.4 A/W for the northwest (NW) quadrant. The northeast (NE) and southwest (SW) quadrants exhibited maximum responsivities of 15.4 A/W and 19.9 A/W, respectively. These values exceed the native responsivity of silicon by more than an order of magnitude [8], highlighting the substantial gain achievable with the graphene-silicon detector architecture. Moreover, based on the underlying device physics, responsivity is expected to increase at lower laser powers, further enhancing gain and signal for low-flux applications [4,5].

4.5.3 Laser Position Sensitivity

To characterize the positional response of the silicon-graphene quadrant detector, one-dimensional center cuts along the X and Y axes were extracted from a small raster scan of the device. The normalized position signals, X_{pos} and Y_{pos}, were calculated according to the standard quadrant detector formula:

$$X_{pos} = \frac{(A+D)-(B+C)}{(A+B+C+D)} \tag{4.1}$$

$$Y_{pos} = \frac{(A+B)-(C+D)}{(A+B+C+D)} \tag{4.2}$$

where A, B, C, and D represent the calibrated signal response of the SW, SE, NE, and NW quadrants, respectively. The resulting signals are nondimensional, as they are normalized by the total intensity, and all sensitivities reported here correspond to the slope of this normalized response versus displacement.

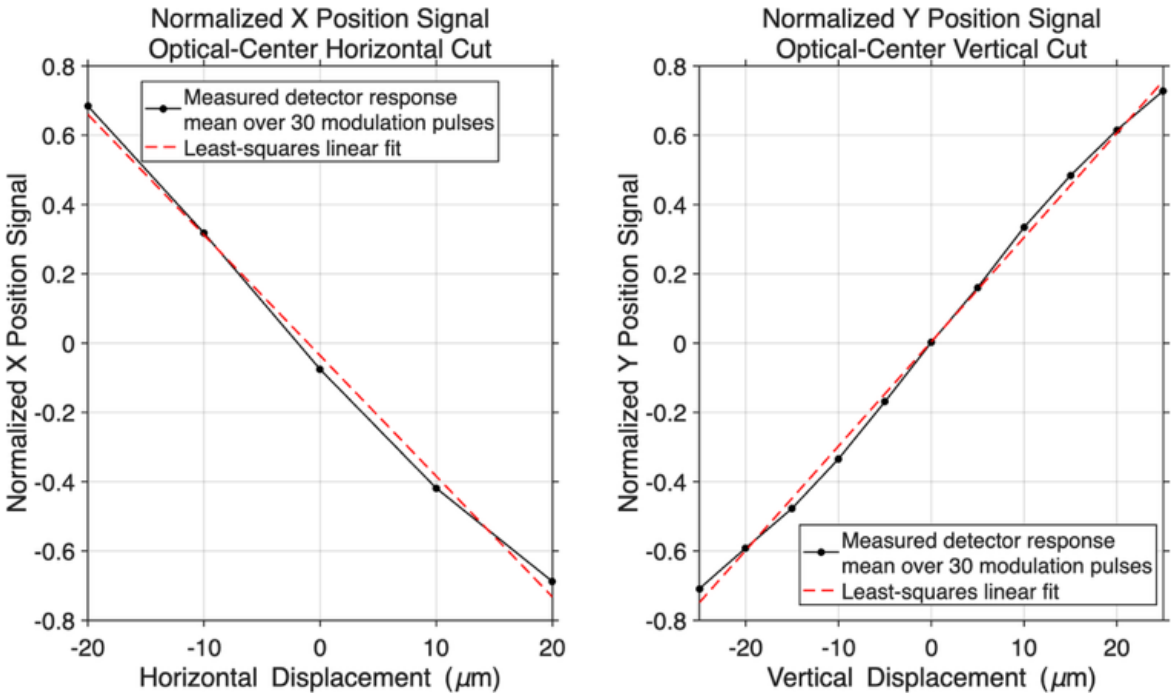


Figure 34. (**Left**) Normalized X position signal as a function of horizontal displacement along the optical-center cut of the quadrant detector. (**Right**) Normalized Y position signal as a function of vertical displacement along the optical-center cut. Each plotted data point represents the average detector response over 30 modulation pulses. In both panels, the solid black curves represent the measured detector response, while the red dashed lines indicate least-squares linear fits. The slopes of the fits define the normalized position sensitivities, and deviations from linearity are used to quantify the detector nonlinearity. The mean normalized signal standard deviation was 0.0036 for the X-position response and 0.0023 for the Y-position response.

Figure 34 shows the 1D X and Y cuts through the center of the raster scan. The X cut corresponds to the detector response along the horizontal direction at the central Y position, while the Y cut corresponds to the vertical response at the central X position. The raster step sizes used were dx = 10 µm and dy = 5 µm, and the incident laser spot had a diameter of approximately 40 µm. Despite the spot size being larger than the raster increments, the center region of the detector maintains a clear quasi-linear response, allowing accurate extraction of both sensitivity and position resolution from these center-line cuts.

Linear fits were performed over the central region of the raster scan (±20 µm for X, ±25 µm for Y due to the chosen raster step sizes in each direction) to extract the detector sensitivity. The measured sensitivities of the quadrant detector are -3.493×10^{-2} per µm in the X-direction

and 3.009×10^{-2} per μm in the Y-direction, both expressed for the normalized response. The negative slope in the X-direction reflects the coordinate convention used during quadrant rotation and does not affect the magnitude of the response.

The linearity of the detector was quantified as the maximum deviation from a least-squares linear fit, normalized to the full-scale output of the fitted response. The detector exhibits robust linearity, with a nonlinearity of 3.04 % along X and 3.36 % along Y.

The measured zero-magnitude response of the detector is slightly offset from the raster scan center, with the X and Y zero positions occurring at approximately 3 μm and < 1 μm, respectively. These offsets indicate that the electrical or optical center of the detector does not necessarily coincide with the mechanical origin of the raster scan. Such shifts may arise from mechanical misalignment between the laser beam and the detector center, mounting tolerances, or intrinsic asymmetries in the quadrant detector layout. While these offsets do not affect the slope of the linear response, they represent the lateral displacement of the detector's true center relative to the scan coordinates and should be considered in applications requiring absolute position calibration.

4.6 Conclusion & Future Work

We developed a novel graphene-silicon quadrant photodetector architecture that enables true multi-pixel integration while preserving the high photoconductive gain of graphene-silicon heterojunctions. We show that the use of L-shaped graphene strips and symmetric electrode placement yields uniform quadrant response, low cross-talk, and responsivities up to ~23 A/W, about thirty times greater than conventional silicon quad-cells. These results establish graphene-silicon heterostructures as a potential pathway to high-sensitivity, low-voltage quadrant detectors compatible with standard silicon processing and readout electronics. Future work should focus on

substrate engineering, improved graphene material quality, and optimized fabrication processes to further enhance uniformity, scalability, and detector performance.

4.7 References

[1] Marktech Optoelectronics, Quadrant and Array Photodiodes, Marktech Optoelectronics, Latham, NY, USA. [Online]. Available: https://marktechopto.com/detectors/quadrant-array-photodiodes/. Accessed: May 1, 2024.

[2] Thorlabs, Inc., Photodiodes, Thorlabs, Inc., Newton, NJ, USA. [Online]. Available: https://www.thorlabs.com/newgrouppage9.cfm?objectgroup_id=285. Accessed: 2024.

[3] Thorlabs, Inc., PDQ80A Quadrant Detector Sensor Head (400–1050 nm), Thorlabs, Inc., Newton, NJ, USA. [Online]. Available: https://www.thorlabs.com/thorproduct.cfm?partnumber=PDQ80A. Accessed: 2024.

[4] K. Liu and S. Kar, "High-Gain Graphene-Silicon Heterojunction Photodetectors Enabled by Quantum Carrier Reinvestment," ACS Nano, vol. 8, no. 6, pp. 5653–5662, 2014. [Online]. Available: https://doi.org/10.1021/nn503484s

[5] X. An, F. Liu, Y. J. Jung, and S. Kar, "Tunable Graphene-Silicon Heterojunctions for Ultrasensitive Photodetection," Nano Lett., vol. 13, no. 3, pp. 909–916, Jan. 2013. [Online]. Available: https://doi.org/10.1021/nl303682j

[6] F. G. De Geronimo and N. O. Renno, "Low-noise stabilization mechanism to enhance the performance of high-gain silicon-graphene photodetectors," *IEEE Sensors Letters*, vol. 9, no. 12, pp. 1–4, Dec. 2025. doi:10.1109/lsens.2025.3633998

[7] J. H. Gosling, O. Makarovsky, F. Wang, N. D. Cottam, M. T. Greenaway, A. Patanè, R. D. Wildman, C. J. Tuck, L. Turyanska, and T. M. Fromhold, "Universal mobility characteristics of graphene originating from charge scattering by ionised impurities," Commun. Phys., vol. 4, no. 1, 2021. [Online]. Available: https://doi.org/10.1038/s42005-021-00518-2

[8] S. M. Sze and K. K. Ng, Physics of Semiconductor Devices, 3rd ed. Hoboken, NJ, USA: John Wiley & Sons, 2007.

[9] Excelitas Technologies, "C30845EH Silicon PIN 4-Quadrant Photodiode," Datasheet. Available: https://www.excelitas.com/product/c30845eh-si-pin-8mm-8-quadrant

Chapter 5 Conclusion and Future Investigations

In this chapter, we summarize the key contributions, limitations, and future directions of the research presented in this dissertation. We begin with a summary of the three major contributions of the research, followed by a discussion of the current limitations of the silicon-graphene photodetector architecture, and conclude with potential directions for future investigations.

5.1 Summary of Key Contributions

This thesis presents the development, characterization, and enhancement of the hybrid silicon-graphene photodetector architecture for high-sensitivity and low-noise optical sensing applications. Throughout this research, the focus has been on addressing the trade-off between responsivity and noise in the silicon-graphene photodetectors and extending these detectors into multi-pixel arrays.

My major contribution was **the development, fabrication and experimental validation of the hybrid silicon-graphene photodetector architecture**. A single-pixel silicon-graphene photodetector was designed and fabricated using standard silicon processing techniques combined with graphene transfer and patterning. The fabrication process was carefully iterated and tuned to improve device yield and performance. The resulting devices demonstrated high responsivity under low optical power conditions, consistent with (and at times outperforming) the literature. These results confirmed the robustness of the fabrication process I developed and the effectiveness of the hybrid silicon-graphene photodetector architecture.

The second and central contribution of my research was **the development of a low-noise stabilization mechanism for these detectors**. By actively regulating the operating point of the graphene channel, the stabilization circuit reduced the detector's sensitivity to environmental perturbations while maintaining high-gain, high-frequency photoresponse. Experimentally, this approach resulted in a reduction in dark current noise power by a factor of approximately 2–4x over a temperature range from -5°C to 55°C, and up to ~4x reduction in noise under modulated optical excitation in the presence of parasitic background illumination. Importantly, this improvement is achieved without measurable loss in optical gain, demonstrating that stability and high responsivity can be simultaneously maintained.

The third major contribution of my research was **the extension of the stabilized graphene-silicon architecture to a true quadrant detector geometry**. A novel L-shaped graphene strip configuration was introduced to enable adjacent detectors while maintaining the high-gain characteristics of hybrid silicon-graphene photodetectors. This enabled the development of a multi-pixel graphene-silicon detector with measured responsivities ranging from approximately 10 to 23 A/W per quadrant, significantly exceeding conventional silicon photodetectors. The device also demonstrated low pixel cross-talk (~5%), linear position sensitivity, and rotational symmetry, validating its suitability for precision optical alignment applications.

Collectively, these contributions establish a framework for the development of graphene-enhanced detectors while identifying clear avenues for the optimization and continued development of the technology.

5.2 Limitations of Current Achievements

Despite the improvements in the performance of graphene-enhanced detectors demonstrated in this thesis, several limitations remain and define future opportunities for improvement.

First, device performance remains sensitive to variability in graphene material quality. Mechanical defects such as folding, tearing, and non-uniform strain in the PMMA/graphene stack during the wet transfer process can introduce significant device-to-device variations in mobility and contact resistance. This effect was evident in the fabrication of our quadrant detector, where dark current noise differed noticeably across quadrants. Nevertheless, the responsivity and high-gain behavior remained comparable between quadrants, ultimately enabling successful device operation.

Second, the fabrication of silicon-graphene detectors is inherently delicate due to the requirement that devices be processed on small, discrete silicon pieces rather than full wafers. This constraint is driven by the graphene transfer and deposition process, which is typically better suited to limited-area substrates where alignment, handling, and contamination control can be more tightly managed. However, this piece-based approach introduces significant handling complexity and reduces compatibility with standard semiconductor processing workflows, most of which are optimized for wafer-scale fabrication. Transitioning to wafer-level fabrication would substantially simplify processing by enabling the use of conventional lithography tools, automated alignment systems, and batch processing equipment, thereby improving reproducibility, scalability, and overall manufacturing efficiency.

Third, although the stabilization mechanism significantly improves noise performance, it also limits the bandwidth of the device due to the mitigation of low-frequency fluctuations. This

constrains the use of this system to higher-frequency applications based on the chosen electronic components of the circuit. A tradeoff study between stabilization strength and temporal response is essential for use of this system in low-frequency applications.

Finally, existing models of the high-gain mechanism present in our silicon-graphene detectors remain incomplete when applied to full device systems. In particular, the dependence of responsivity on incident power, graphene mobility variation, environmental effects, and other quantum capacitance effects are not fully captured in the current framework. A more comprehensive model would improve predictive accuracy and future device optimization.

5.3 Recommendations for Future Studies

While the results presented in this thesis represent significant advancements in silicon-graphene photodetector and quadrant detector technologies, several important improvements remain for future investigations.

A primary direction is the scaling of the current quadrant detector architecture to larger format arrays. While the current system is a four-pixel implementation, future systems could leverage the same L-shaped graphene strips, or stacked architectures, to enable higher-density arrays. This would require careful optimization of interconnect routing, pixel uniformity across the entire device, and wafer-scale fabrication processes. Future investigations could open the application space of this technology significantly, moving into full image-producing systems.

A second direction for future investigations would be improvements in the graphene deposition process. The current wet transfer process can introduce defects and variability between samples. Using CVD-grown graphene — typically synthesized on copper foil and subsequently transferred — offers significantly better crystalline quality, larger domain sizes, and more uniform electrical characteristics than exfoliated or commercially available PMMA-supported films.

Pairing CVD graphene with a dry transfer process could further reduce interface contamination introduced during transfer. Together, these improvements could enhance carrier mobility, reduce trap state density at the silicon-graphene interface, lower dark current noise, and yield more consistent device-to-device performance across fabrication runs.

Third, packaging the stabilization circuit into a compact, purpose-built PCB would be a critical step toward practical deployment. The current breadboard implementation occupies considerable bench space and relies on long wired connections to the detector, introducing susceptibility to electromagnetic pickup, parasitic capacitance, and ground loops that can degrade noise performance. A dedicated PCB would not only shrink the system footprint but also shorten signal paths, improve impedance control, and reduce environmental interference — directly benefiting the low-noise operation that the stabilization mechanism is designed to achieve. Such a package would also present a well-defined electrical and mechanical interface, making integration into larger optical instruments or spacecraft payloads substantially more straightforward.

A fourth investigation could focus on improving device robustness through passivation layers and additional fabrication steps. Because graphene-based devices are highly sensitive to surface adsorbates, ambient humidity, contamination, and processing residues, the detector response may drift under changing environmental conditions. Introducing a suitable passivation layer, such as an Si_3N_4 transparent layer, could help isolate the graphene channel and exposed device interfaces from the surrounding environment, reducing unwanted fluctuations while preserving optical access to the active silicon region. Additional fabrication refinements, such as improved cleaning protocols, optimized contact deposition, or encapsulation of vulnerable interfaces, could further enhance device-to-device consistency, long-term stability, and operational reliability. These improvements would be especially important for translating the detector from

controlled laboratory testing to practical deployment in field, industrial, or spacecraft environments.

Finally, as mentioned in Section 5.2, future research should focus on further developing the theoretical framework surrounding these devices and their operation in different environments. A unification of the electrical, optical, and thermal behavior of graphene-silicon photodetectors under a single predictive framework would enable more accurate predictions of gain stability, noise behavior, and bandwidth limitations under varying environmental and optical conditions.

5.4 Final Remarks

This thesis reports the successful development of silicon-graphene photodetectors and quadrant detector architectures for high-sensitivity optical sensing applications. By integrating graphene into silicon-based device platforms, our research establishes a pathway toward photodetectors that combine high responsivity, low power consumption, and compatibility with scalable semiconductor fabrication processes.

The introduction of a low-noise stabilization mechanism and a novel quadrant detector geometry further demonstrate the versatility of silicon-graphene heterostructures for both single-pixel and position-sensitive detection applications.

While additional research is required to improve scalability, long-term stability, and integration, this thesis provides a strong foundation for future development of graphene-enhanced optoelectronic systems. Continued progress in fabrication techniques, device modeling, and system integration is expected to further enhance the performance and applicability of these technologies in scientific, industrial, and aerospace sensing applications.